Yonis Hakim

Dr. Chetan Patil & Dr. Michel Lemay

Honors Scholars Project

December 17, 2018

Evaluation of Transcranial NIR Light Propagation for Photo-biomodulation of Neurons Using Mesh-Based Monte Carlo Modeling

Abstract

Research has shown that photo-biomodulation of neurons with near-infrared (NIR) light can stimulate their regeneration, and thus various research groups have developed devices that emit NIR light transcranially (through the skull) to stimulate neural growth in the brain in an effort to treat neurological diseases such as Multiple Sclerosis (MS) and Alzheimer's. However, it is not clear that clinical device designs illuminate cells in the brain with similar parameters as those shown effective for neuro-regeneration in pre-clinical work. This project employed computational modeling and simulations to assess the effect of device design parameters on transcranial light propagation, in order to optimize illumination of brain tissue and cells and thus ultimately improve clinical results of transcranial NIR-emitting devices for neuro-regeneration. Specifically, this project consisted of the development of two computational models for

transcranial NIR-emitting devices and the evaluation of three device parameters: wavelength, photon number, and power density, on transcranial NIR light propagation.

Table of Contents

Abstract 1

Table of Contents 2

Introduction 7

Problem and Overview 7

Optical Properties of the Human Head in the Literature 10

Anderson and Parrish (1981) 10

Jacques, Alter, and Prahl (1987) 10

Marchesini, Bertoni, Andreola, Melloni, and Sichirollo (1989) 11

Splinter, Cheong, van Gemert, and Welch (1989) 11

Sterenborg, Van Gemert, Kamphorst, Wolbers, and Hogervorst (1989) 11

Van Gemert, Jacques, Sterenborg, and Star (1989) 12

Cheong, Prahl, and Welch (1990) 12

Van der Zee (1992) 13

Firbank, Hiraoka, Essenpreis, and Delpy (1993) 13

Graaff et al. (1993) 13

Tearney et al. (1995) 14

Chan et al. (1996) 14

Matcher, Cope, and Delpy (1997) 14

Okada et al. (1997) 15

Dögnitz and Wagnières (1998) 15

Firbank, Okada, and Delpy (1998) 15

Simpson, Kohl, Essenpreis, and Cope (1998) 15

Bevilacqua et al. (1999) 16

Doornbos, Lang, Aalders, Cross, and Sterenborg (1999) 16

Rajadhyaksha, González, Zavislan, Anderson, and Webb (1999) 16

Meglinsky and Matcher (2001) 17

Tauber, Baumgartner, Schorn, and Beyer (2001) 17

Troy and Thennadil (2001) 17

Yaroslavsky et al. (2002) 17

Fukui, Ajichi, and Okada (2003) 18

Iino et al. (2003) 18

Okada and Delpy (2003, 1) 18

Okada and Delpy (2003, 2) 19

Popp, Valentine, Kaplan, and Weitz (2003) 19

Franceschini and Boas (2004) 19

Bashkatov, Genina, Kochubey, and Tuchin (2005) 19

Boas and Dale (2005) 19

Koyama, Iwasaki, Ogoshi, and Okada (2005) 19

Bashkatov, Genina, Kochubey, and Tuchin (2006) 20

Custo, Iii, Barnett, Hillman, and Boas (2006) 20

Ding, Lu, Wooden, Kragel, and Hu (2006) 20

Gebhart, Lin, and Mahadevan-Jansen (2006) 20

Mudra, Nadler, Keller, and Niederer (2006) 21

Salomatina, Jiang, Novak, and Yaroslavsky (2006) 21

Comelli et al. (2007) 21

Schneiderheinze, Hillman, and Sampson (2007) 22

Tseng, Grant, and Durkin (2008) 22

Mansouri, L'Huillier, Kashou, and Humeau (2010) 22

Bashkatov, Genina, and Tuchin (2011) 22

Haeussinger et al. (2011) 25

Li, Gong, and Luo (2011) 25

Sandell and Zhu (2011) 25

Kurihara et al. (2012) 25

Lister, Wright, and Chappell (2012) 25

Jacques (2013) 26

Strangman, Li, and Zhang (2013) 27

Farina et al. (2015) 27
Li, Zhao, Sun, and Li (2015) 28
Pitzschke et al. (2015) 28
Yue and Humayun (2015) 28
Yue et al. (2015) 28
Li, Xue, Wang, Li, and Wu (2017) 28
Materials and Methods 29
Materials 29
Methods 29
Results 30
Head and Brain Mesh 30
Simulations Using 630 nm Head Model 31
Simulations Using 650-800nm Head Model 31
Simulations of Varying Photon Number 31
Simulations of Various Wavelengths 32
Simulations of Various Power Density 32
Simulations Using 785 nm Clinical Study Light Source 33
Time to Perform the Various Simulations 33
Discussion 33
Expected Clinical Results 33

Application to Clinical Devices 35

Limitations 36

Conclusion 36

Acknowledgments 37

Appendices 37

Appendix A: Results 37

Head and Brain Mesh 37

Head Mesh 38

Head with Brain Shown 38

Simulations Using 630 nm Head Model 39

Inputs for 630 nm Head Model 39

Fluence of Light at 630 nm Wavelength and 30 Million Photon 40

Simulations Using 650-800nm Head Model 41

Inputs for 650-800 nm Head Model 41

Simulations of Varying Photon Number 42

Simulations of Various Wavelengths 45

Simulations of Various Power Density 47

Simulations Using 785 nm Clinical Study Light Source 49

Time to Perform the Various Simulations 50

Light Penetration Lengths of the Simulations 51

Appendix B: Discussion 51
Clinical NIR-Emitting Devices' Parameters 51
Appendix C: Photobiomodulation on a Cellular and Tissue Level 52
In vitro Photobiomodulation 52
Effect of Light on Cells and Tissue 55
References 56

Introduction

Problem and Overview

Photobiomodulation is illuminating tissues with blue light (450-495 nm), green light (500-570 nm), red light (600-700 nm), and/or near-infrared (NIR) light of 760-1200 nm to stimulate the tissue to repair, grow, and regenerate. Most of photobiomodulation studies employ the "optical window," which is the wavelengths at which light's tissue penetration is maximized, and this window is around 600-1070 nm. Further, photobiomodulation can be used to treat a variety of diseases and disorders, from which are brain disorders, neck and joint pain, wounds, mucositis, and many others. Regarding brain disorders, which are the interest in this project, that photobiomodulation treats, they are classified into three categories, traumatic events which include stroke and Traumatic Brain Injury (TBI), degenerative diseases which includes Alzheimer's disease, and psychiatric disorders which include depression and post-traumatic stress (Salehpour et al., 2018).

Upon illumination with light, the brain responds in different ways. It Increases neovascularisation and structural protein synthesis, such as collagen, to repair tissue damage and promote healing of wounds. Also, it Increases cell proliferation of fibroblasts, keratinocytes, endothelial cells, and lymphocytes *in vitro*. In addition, it reduces pain and inflammation, and it increase blood flow (Salehpour et al., 2018).

Photobiomodulation works by getting advantage of the biphasic dose response, which is a biological law stating that biological systems are stimulated by low doses of any physical/chemical stimuli, regardless of its toxicity or harm. If very low energy is applied, the minimum threshold is not reached and no response will result. If more energy is applied, the threshold is crossed, resulting in biostimulation until a peak is reached. If even more energy is applied, bioinhibition occurs, resulting in less benefit. However, if a lot of energy is applied above the threshold, damage to the cells occurs (Salehpour et al., 2018).

Multiple research groups have employed photobiomodulation in pre-clinical (in vitro and in vivo) and clinical studies. Clinically, various research groups have developed devices that emit NIR light transcranially (through the skull) to stimulate neural growth in the brain in an effort to treat neurological diseases, such as Multiple Sclerosis (MS) and Alzheimer's. These clinical devices employed different parameters than those used in pre-clinical work, and the parameters that they used varied from a study to another. Indeed, the designs of these devices included different parameters, including power density, energy density, time of illumination, area of illumination, and wavelength. The values of these parameters varied widely between studies. The range of power density used in transcranial brain photobiomodulation studies ranges between 10-30 mW/cm2 in LED light sources and reached 700 mW/cm2 in lasers. Although the power densities employed reached high values, they do not cause severe skin reaction. Indeed, studies

have shown that heating of the skin is perceptible at a power density of 500 mW/cm2 and becomes severe at 1 W/cm2. Since the power densities employed do not reach this magnitude, they do not result in a severe skin heating. As for energy density, it ranged between 10-137.5 J/cm2. Regarding the time of illumination, it ranges from 10 sec to more than 10 min. Moreover, the area exposed to light ranges from 1 cm2 to more than 137 cm2. Regarding wavelengths employed, they varied widely as was mentioned earlier. However, NIR light was shown to be most profitable (Salehpour et al., 2018).

Concerning these wide ranges of values used for the parameters of the transcranial NIR-light emitting devices, it is not clear that clinical device designs illuminate cells in the brain with similar parameters as those shown effective for neuro-regeneration in pre-clinical work, and so it is also unclear which of these parameters optimize neuronal cell growth and generation to better treat neurological disorders and diseases. Hence, this project used computational modeling and simulations to set guidelines for specifying device design parameters that could optimize illumination of cells and neuronal regeneration, and thus ultimately improve clinical results of transcranial NIR-emitting devices for neuro-regeneration. These device guidelines may be used in the future for developing a transcranial NIR-emitting device that results in optimal neuro-regeneration. The optimization of cell illumination and neuronal regeneration was defined by the largest penetration depth and the largest particle flux, or fluence, under the least Maximal Permissible Exposure (MPE) level in the skin. In addition, computational modeling and simulations were performed using Mesh-based Monte Carlo (MMC), which is a powerful computational technique used in biomedical optics used to perform modeling and simulations of photon migration in the complex three-dimensional (3D) structures, such as that of the brain (Fang, 2010).

Using MMC, two head models were constructed to study the effect of three of the most important parameters involved in the designs of transcranial NIR light-emitting devices, wavelength, power density, and the total number of photons illuminated. Using MMC the effect of these parameters was studied to set guidelines for the specification of NIR light-emitting devices parameters.

Optical Properties of the Human Head in the Literature

In order to perform simulations of NIR light propagation through the head, the optical properties of the human head must be known because they affect how light is absorbed, scattered, and transmitted through the different tissues. The following studies provided optical properties of the human head, either by performing experiments on actual tissue, by estimating these properties using computational modelling, or by using optical properties obtained from the literature.

Anderson and Parrish (1981)

Anderson and Parrish (1981) provided the optical properties of the human skin using Kubelka-Munk modelling, reporting the absorption and reduced scattering coefficients of *in vitro* 200 μm thick human dermis at 300-2400 nm.

Jacques, Alter, and Prahl (1987)

Jacques et al. (1987) investigated the optical properties of *in vitro* human skin obtained from Caucasian subjects of 50-70 years old. The authors performed three experiments. In one of the experiments, shin skin was obtained from the subjects with a thickness of 200-650 μm, where the dermis was approximately 100 μm thick. These samples were soaked in a normal saline solution

with 85% water to hydrate. In the second experiment, they obtained abdomen skin from the subjects, having dermal samples of 200-400 μm thickness. These samples were soaked in a saline solution. In the third experiment, they had abdomen dermal samples of 20 μm thickness and stacked them so that the total thickness is 20-100 μm, with a step size of 20 μm. Moreover, the authors reported the index of refraction and the anisotropy factor for these samples. They measured the anisotropy factor using two methods. First, goniometric experiments along with the Henyey-Greenstein method. Second, using an integrating sphere experiments along with the diffuse approximation method.

Marchesini, Bertoni, Andreola, Melloni, and Sichirollo (1989)

Marchesini et al. (1989) provided the absorption and scattering coefficients of the human dermis at 635 nm. They used an integrating sphere to collect transmittance and reflectance data. Then, they used the Henyey-Greenstein to reach the optical coefficients. Also, they used dermis from the leg with a thickness of 20-100 μm and area of approximately 1 cm^2.

Splinter, Cheong, van Gemert, and Welch (1989)

Splinter et al. (1989) provided the optical properties of the human brain *in vitro*. The authors of the study obtained a human cadaver's brain and kept in cold saline solution and in an ice bath. Then, without fixing the sample, it was sectioned unfrozen using a scalpel. This study provided the absorption coefficient, the scattering coefficient, the anisotropy factor, the total diffuse transmittance, the diffuse reflectance, and the total collimated transmission of the human cadaver brain at 632.8 nm.

Sterenborg, Van Gemert, Kamphorst, Wolbers, and Hogervorst (1989)

Sterenborg et al. (1989) provided the transport absorption and scattering coefficients of the human grey and white matter *in vitro* at 400-1100 nm using diffusion approximation.

Van Gemert, Jacques, Sterenborg, and Star (1989)

Van Gemert et al. (1989) provided the index of refraction of the human skin. The authors' work also reported the anisotropy factor of each of the stratum corneum, the epidermis, and the epidermis at 240-633 nm. For the stratum corneum, it reported the results of another research study at 240-400 nm for the anisotropy factor. In addition, it reported the results of a second study for the value of the anisotropy factor of the stratum corneum, for the anisotropy factor of the epidermis at 300 nm and 540 nm, and for the experimental absorption and scattering coefficients for the stratum corneum, the epidermis, and the dermis at 200-800 nm.

Cheong, Prahl, and Welch (1990)

Cheong et al. (1990) provided the optical properties of the human adult brain, the stratum corneum, and the dermis. The study provided the absorption coefficient and reduced scattering coefficient of the human adult brain postmortem at 630 nm, using the Kubelka-Munk method to determine the coefficients. It also reported the absorption coeffiecient of the dermis at 630 nm, using an integrating sphere, a goniophotometer, and Beer's Law. In addition, it reported the absorption coefficient, the scattering and reduced scattering coefficients, and the anisotropy factor for the dermis at 633 nm, using a goniophotometer, diffusion theory, and the Henyey equation. Moreover, the absorption coefficient and reduced scattering coefficient of the dermis at 635 nm were reported, using an integrating sphere, a goniophotometer, and Beer's Law. Additionally, the absorption coefficient of the stratum corneum at 193 nm was reported using Beer's Law.

Van der Zee (1992)

Van der Zee (1992), in his doctorate dissertation, provided a review of the optical properties of various human tissue in the NIR range. His dissertation provided the absorption coefficient and reduced scattering coefficient for the adult human brain at 700-900 nm. In addition, it provided the absorption and scattering coefficients of the stratum corneum at 254-546, its index of refraction at a thickness of 8-15 μm, and its anisotropy factor. Moreover, this work provided the absorption and scattering coefficients of the epidermis minus the stratum corneum at the visible range, also providing anisotropy factor. Also, the absorption and scattering coefficients and the anisotropy factor were provided for the dermis.

Firbank, Hiraoka, Essenpreis, and Delpy (1993)

Fibrank et al. (1993) investigated the optical properties of a pig's skull. The study employed a goniometer to measure the scattering phase function. It also used two integrating spheres, the Newton Raphson technique, and Monte Carlo modelling to find the absorption and scattering coefficients, the diffuse reflectance, and the transmittance of the samples. It reported the absorption and scattering coefficients, the reduced scattering coefficient, and the anisotropy factor at 650-950 nm.

Graaff et al. (1993)

Graff et al. (1993) provided the anisotropy factor of the dermis at 300-1300 nm, the refractive index of the skin, and the absorption and reduced scattering coefficients of the dermis at 633 nm. For the optical coefficients the diffusion approximation and Monte Carlo methods were used to obtain the values. The authors also provided the absorption and reduced scattering coefficients of

the dermis of white and dark skin at 700, 950, and 1230 nm, using Monte Carlo simulations. In addition, they provided the absorption and scattering coefficients, the reduced scattering coefficient, and the anisotropy factor of the dermis at 633 nm, using the adding-doubling method. Moreover, they provided the absorption and reduced scattering coefficients of the dermis at 633 nm using the Monte Carlo method. For bloodless dermis, they provided the absorption and reduced scattering coefficients at 660 nm and 950 nm.

Tearney et al. (1995)

Tearney et al. (1995) determined the refractive index for *in vitro* dermis, *in vivo* stratum corneum, *in vivo* epidermis, and *in vitro* human tissue postmortem, including human dermis. They used two methods to find the refractive index. In one method, they used optical coherent tomography to measure optical path length refractive index. In the second method, they used focus tracking. Moreover, they dissected the samples to 500 μm and used a super luminescent diode possessing a bandwidth of 50 nm and a center wavelength of 1300 nm.

Chan et al. (1996)

Chan et al. (1996) provided the absorption coefficient and the reduced scattering coefficient of skin at 400-1800 nm. The used skin was postmortem from the buttocks and hind leg. The number of samples was 53 from Caucasian males, 72 from Caucasian females, and 35 from Hispanic males. In addition, the authors used an IR spectrophotometer, the integrating sphere method, and the inverse adding-doubling method to determine the optical coefficients.

Matcher, Cope, and Delpy (1997)

Matcher et al. (1997) provided the absorption coefficient of forearm, calf, and head tissue at 800 nm and 760-900 nm. They also provided the absorption and reduced scattering coefficients of the grey matter at the same wavelength.

Okada et al. (1997)

Okada et al. (1997) provided the absorption and reduced scattering coefficients of the scalp + skull, cerebrospinal fluid, grey matter, and white matter at 800 nm.

Dögnitz and Wagnières (1998)

Dögnitz and Wagnières (1998) used skin from 6 subjects to report the absorption and reduced scattering coefficients of skin at 400, 500, 633, and 700 nm. The authors illuminated the samples with spatially and periodically modulated light. Then, backscattered light and reflectance were used to obtain these optical coefficients using Monte Carlo.

Firbank, Okada, and Delpy (1998)

Firbank et al. (1998) provided the absorption and reduced scattering coefficients of the skin + skull, cerebrospinal fluid, grey matter, and white matter at 800 nm.

Simpson, Kohl, Essenpreis, and Cope (1998)

Simpson et al. (1998) reported the optical properties of *ex vivo* human skin. This study used the single integrating sphere technique to measure the reflectance and transmittance of the samples. Then, the Monte Carlo inversion technique was used to determine the optical coefficients. Moreover, the study used human abdominal and breast tissue to obtain 1.5-2 mm thick samples of the dermis with the epidermis and 2 mm thick samples of the subdermis. The samples were

discs and had a diameter of 16 mm, and they were from 4 Caucasian subjects and one African American subject. Furthermore, the study reported the absorption coefficient and the reduced scattering coefficient at 620-1000 nm for Caucasian dermis and subdermis and African American dermis, specifically stating these values at 633, 660, 700, 749, 789, and 836 nm. Additionally, this study reported the refractive index and the anisotropy factor of the skin.

Bevilacqua et al. (1999)

Bevilacqua et al. (1999) reported the absorption coefficient and the reduced scattering coefficient of the *in vivo* skull and cerebral white matter at 674, 849, and 956 nm. The authors used Monte Carlo simulations to determine the coefficients for the reflectance data that they obtained from the samples, which represent a homogeneous semi-infinite turbid media.

Doornbos, Lang, Aalders, Cross, and Sterenborg (1999)

Doornbos et al. (2001) providd the absorption and reduced scattering coefficient of *in vivo* white skin at 633, 660, and 700 nm. The authors calculated the reflectance spectrum at the different source-detector distances they used. Then, they obtained optical coefficients from the spectrum by using the diffusion approximation. Next, they used Mie-like scattering function to recalculate the optical properties. In addition, they reported from the literature data the absorption and reduced scattering coefficients of *in vivo* skin from the arm, foot sole, and forehead at 500-1000 nm specifically providing the values at 633, 660, and 700 nm.

Rajadhyaksha, González, Zavislan, Anderson, and Webb (1999)

Rajadhyaksha et al. (1999) provided the refractive index of the stratum corneum, epidermis, and dermis.

Meglinsky and Matcher (2001)

Meglinsky and Matcher (2001) provided the anisotropy factor, index of refraction, absorption coefficient, and reduced scattering coefficient at 600 nm using Caucasian skin samples, reporting the values for the stratum corneum, living epidermis, papillary epidermis, upper blood net dermis, dermis, deep blood net dermis, and subcutaneous fat tissue.

Tauber, Baumgartner, Schorn, and Beyer (2001)

Tauber et al. (2001) reported the absorption coefficient and the reduced scattering coefficient of the petrous bone, maintained in a formalin solution. This study used a CCD camera to measure reflectance and absorption then Monte Carlo calculations determine the optical coefficients, which were reported at 593, 635, 690, 780, and 830 nm. In addition, the authors reported the refractive index and the anisotropy factor of the bone.

Troy and Thennadil (2001)

Troy and Thennadil (2001) used a double integrating sphere to collect diffuse transmittance and reflectance data, and they determined the absorption and isotropic scattering coefficient using the inverse adding-doubling method. They used 22 skin samples from 14 subjects from the scalp, leg, and groin. The samples were either inflamed, damaged, or normal in condition, and they were maintained in a saline solution. Using their experiment, they reported the absorption and reduced scattering coefficient of the skin at 1000-2200 nm, specifically stating the values at 1000, 1460, 1600, and 2200 nm. The authors also reported the anisotropy factor and refractive index at 1000-2200 nm from the literature.

Yaroslavsky et al. (2002)

Yaroslavsky et al. (2002) provided the optical properties of native and coagulated *in vitro* white and grey matter, cerebellum, pons, and thalamus tissue at 360-1100 nm. The samples were coagulated by heating them in a saline solution. Moreover, to measure the diffuse reflectance, total transmittance, and collimated transmittance, the integrating sphere technique was used. Then, the inverse Monte Carlo technique was employed to determine the absorption and scattering coefficients and the anisotropy factor. The white matter was 80-150 μm, and the grey matter was 100-200 μm. Additionally, the study specifically reported the absorption and scattering coefficients, anisotropy factor, and the reduced scattering coefficient for native white matter at 456, 450, 510, 514, 630, 675, 670, 850, and 1064 nm. It provided the values for these variables for native grey matter at the same wavelengths, except 850 nm. For coagulated white matter, the study specifically reported the values for these variables at 850 nm and 1064 nm.

Fukui, Ajichi, and Okada (2003)

Fukui et al. (2003) provided the absorption coefficient and reduced scattering coefficient of the scalp, skull, cerebrospinal fluid, grey matter, and white matter at 800 nm.

Iino et al. (2003)

Iino et al. (2003) provided the absorption coefficient of the epidermis, dermis, and subcutaneous tissue at 1000-1900 nm. The study also provided the index of refraction and anisotropy factor of the skin.

Okada and Delpy (2003, 1)

Okada and Delpy (2003, 1) provided the absorption and transport scattering coefficients of the scalp, skull, cerebrospinal fluid, grey matter, and white matter at 800 nm.

Okada and Delpy (2003, 2)

Okada and Delpy (2003, 2) provided the absorption and reduced scattering coefficients of the scalp, skull, cerebrospinal fluid, grey matter, and white matter at 800 nm.

Popp, Valentine, Kaplan, and Weitz (2003)

Popp et al. (2003) provided the anisotropy factor of porcine skin.

Franceschini and Boas (2004)

Franceschini and Boas (2004) provided the absorption and reduced scattering coefficients of the scalp, skull, cerebrospinal fluid, grey matter, and white matter.

Bashkatov, Genina, Kochubey, and Tuchin (2005)

Bashkatov et al. (2005) reported the absorption coefficient and the reduced scattering coefficient of skin, subcutaneous adipose tissue, and mucous tissue at 400-2000 nm. The authors used a single integrating sphere to measure reflectance and transmittance, then they used the inverse adding-doubling method to obtain the optical coefficients. The samples were obtained from *in vitro* postmortem skin and from the peritoneum, and they were maintained in a saline solution set at 20 Celsius.

Boas and Dale (2005)

Boas and Dale (2005) provided the absorption and reduced scattering coefficients of the scalp, skull, cerebrospinal fluid, and grey matter + white matter.

Koyama, Iwasaki, Ogoshi, and Okada (2005)

Koyama et al. (2005) provided the absorption coefficient and reduced scattering coefficients at 800 nm for superficial tissue, the cerebrospinal fluid, the grey matter, and the white matter.

Bashkatov, Genina, Kochubey, and Tuchin (2006)

Bashkatov et al. (2006) reported the absorption coefficient and reduced scattering coefficient at 800-2000 nm of *in vitro* 16-70-year-old parietal, temporal, and tempo-parietal skull bones, which were reserve in saline at 5 Celsius temperature. The authors specifically reported these values at 800, 830, 850, 875, 900, 925, 956, 975, 1000 nm. Moreover, a single integrating sphere measured the reflectance and transmittance data then inverse adding-doubling was performed to reach these values.

Custo, Iii, Barnett, Hillman, and Boas (2006)

Custo et al. (2006) provided the absorption and reduced scattering coefficients of the scalp + skull and grey matter + white matter.

Ding, Lu, Wooden, Kragel, and Hu (2006)

Ding et al. (2006) involved *in vitro* skin samples from 12 females of 27-63 years old, from which 10 were Caucasian and 2 were African American. Coherent reflectance curve measurements were taken to provide the refractive index of the epidermis and the dermis at 300-1600 nm.

Gebhart, Lin, and Mahadevan-Jansen (2006)

Gebhart et al. (2006) provided the absorption coefficient and reduced scattering coefficient of *in vitro* white and grey matter at 400-1300 nm. The authors used single integrating sphere technique to measure the reflectance and transmittance of the samples. Then, inverse Monte

Carlo was used to obtain the coefficients. The study used 19 samples of white matter and 25 samples of grey matter of 0.22-1.25 mm thickness.

Mudra, Nadler, Keller, and Niederer (2006)

Mudra et al. (2006) provided the absorption and reduced scattering coefficients of the scalp, skull, cerebrospinal fluid, grey matter, and white matter at 800 nm. The authors also reported the anisotropy factor for the skull, grey matter, and white matter. In addition, they reported the absorption and scattering coefficients, the reduced scattering coefficient, and the anisotropy factor of the skin at 633 nm. Moreover, they provided the absorption and scattering coefficients of the muscle at 515 nm.

Salomatina, Jiang, Novak, and Yaroslavsky (2006)

Salomatine et al. (2006) used an integrating sphere to collect diffuse reflectance and transmittance. Then, the authors used the inverse Monte Carlo method to obtain the absorption and reduced scattering coefficients of the epidermis, dermis, and subcutaneous fat at 400-1600 nm. The experimental data was interpreted assuming that the Henyey-Greenstein function applied, that the refractive index of the skin layers is 1.4, and that the anisotropy factor is 0.8 for the skin layers. The study employed 7 epidermis samples, 8 dermis samples, and 10 subcutaneous fat samples with thicknesses of 60-100 μm, 100-780 μm, and 280-800 μm, respectively.

Comelli et al. (2007)

Comelli et al. (2007) studied the optical properties of *in vivo* forehead. The study employed 5 volunteers, from which 3 where males and 2 were females. The authors collected spectra from

the forehead, then they time-resolved their experimental data to the diffusion approximation of the transport equation for a homogeneous semi-infinite media, assuming a refractive index of 1.4 for the head tissue. They provided the absorption and reduced scattering coefficients of the forehead at 700-1000 nm. They also provided these values for the scalp + skull, the cerebrospinal fluid, the grey matter, and the white matter at 800 nm.

Schneiderheinze, Hillman, and Sampson (2007)

Schneiderheinze et al. (2007) provided the reduced scattering coefficient of the dermis at 400-2000 nm.

Tseng, Grant, and Durkin (2008)

Tseng et al. (2008) provided the absorption and reduced scattering coefficients of Caucasian skin at 650 nm. The authors also used steady-state frequency-domain photon migration in their samples of volar forearm and palm skin from 5 African American subjects, 5 Asian subjects, and 5 Caucasian subjects. They reported the absorption and reduced scattering coefficients of these samples at 650-1000 nm.

Mansouri, L'Huillier, Kashou, and Humeau (2010)

Mansouri et al. (2010) provided the absorption and reduced scattering coefficients, the anisotropy factor, and the refractive index of the scalp, skull, grey matter, and white matter at 759 nm.

Bashkatov, Genina, and Tuchin (2011)

Bashkatov et al. (2011) provided a review of the optical properties of the skin, subcutaneous tissue, and muscle. In their work, they provided the absorption and reduced scattering coefficients of 21 Caucasian skin samples, using a single integrating sphere and the inverse adding-doubling method at 400-2000 nm, with a step size of 100 nm. They also provided these values for 3 Caucasian samples, using the same method for a wavelength range of 400-1800 nm, with a step size of 100 nm. In addition, they provided the values of these optical coefficients for 22 causing skin samples, using a double integrating sphere and the inverse adding-doubling method at 1000-1900 nm, with a step size of 100 nm.

For the stratum corneum, they provided the absorption and scattering coefficients, the reduced scattering coefficient, and the anisotropy factor at 350-700 nm, with a step size of 50 nm. The authors also provided the refractive index at 400-700 nm and 1300 nm.

Moreover, they provided the absorption and scattering coefficients and the anisotropy factor for lightly, medium, and highly-pigmented epidermis at 350-700 nm, with a step size of 50 nm. In addition, the authors reported the absorption and reduced scattering coefficients of 10 human epidermis samples at 400-800 nm, with a step size of 50 nm, using a single integrating sphere and the inverse Monte Carlo method. Additionally, these optical coefficients were given for 7 human epidermis samples at 400-1600 nm, with a step size of 100 nm, using a single integrating sphere and an inverse Monte Carlo method. Furthermore, the authors provided the refractive index for the epidermis at 325, 442, 532, 633, 850, 1064, 1300, 1310, and 1557 nm.

Regarding the dermis, the authors provided the absorption and scattering coefficients and anisotropy factor at 350-700 nm, with a step size of 50 nm. Also, they provided the absorption and reduced scattering coefficients for 8 samples of the human dermis, using a single integrating sphere and the inverse Monte Carlo method at 400-1600 nm, with a step size of 100 nm. For 12

samples of the Caucasian dermis, they provided these optical coefficients, using a single integrating sphere and inverse Monte Carlo at 633 nm and 700-1000 nm, with a step size of 50 nm. In addition, they reported these coefficients for 5 samples of dark skin, using a single integrating sphere and inverse Monte Carlo at 633 nm and 700-1000 nm, with a step size of 50 nm. For Caucasian bloodless dermis, they provided the absorption and scattering coefficients and the anisotropy factor, using a single integrating sphere and the inverse adding-doubling method at 450-800 nm, with a 50 nm step size. Also, they reported the absorption and scattering coefficients, the reduced scattering coefficient, and the anisotropy factor of 5 samples of bloodless Caucasian dermis, using a single integrating sphere and the diffusion approximation method at 633 nm. Additionally, they provided the values for these variables for 30 samples of bloodless Caucasian dermis at 633 nm and 350-450 nm, with 50 nm step size, using the same method. Moreover, they reported the refractive index for the dermis at 325, 442, 532, 633, 850, 1064, 1300, 1310, and 1557 nm.

As for the subdermis, the authors provided the absorption and reduced scattering coefficients for 12 samples of subdrmis, primarily composed of globular fat cells, using the single integrating sphere and inverse Monte Carlo method at 633 nm and 700-1000 nm, with a step size of 50 nm.

Regarding subcutaneous adipose tissue, the authors reported the absorption and reduced scattering coefficients of 6 samples of subcutaneous adipose, using a single integrating sphere and the inverse adding-doubling method at 400-2000 nm, with a step size of 100 nm. They also provided the values for these same optical coefficients for 10 samples of subcutaneous adipose, using a single integrating sphere and the inverse Monte Carlo method at 400-1600 nm, with a 100 nm step size. Moreover, they gave the refractive index of subcutaneous adipose at 456-1064 nm

Haeussinger et al. (2011)

Haeussinger et al. (2011) provided the average of each of the absorption coefficient, scattering coefficient, anisotropy factor, and index of refraction at 650-800 nm for the scalp, skull, cerebrospinal fluid, grey matter, and white matter.

Li, Gong, and Luo (2011)

Li et al. (2011) provided the absorption and scattering coefficients, the anisotropy factor, and the refractive index of the scalp, skull, cerebrospinal fluid, muscle, white matter, grey matter, arterial blood, and venous blood at 800 nm.

Sandell and Zhu (2011)

Sandell and Zhu (2011) provided the absorption and reduced scattering coefficients of the skin at 650-900 nm specifically stating the values at 630, 661, and 800 nm; of the bone at 600-1000 nm specifically stating the values at 650 nm and 760 nm; and of the brain at 420, 532, 630, 760, and 780 nm.

Kurihara et al. (2012)

Kurihara et al. (2012) provided the absorption and transport scattering coefficient of the scalp, skull, cerebrospinal fluid, frontal sinus, grey matter, and white matter at 830 nm.

Lister, Wright, and Chappell (2012)

Lister et al. (2012) provided the absorption and reduced scattering coefficients of the *in vitro* skin, epidermis, and dermis at 350-750 nm. The authors specifically gave the absorption and reduced scattering coefficients of *in vitro* skin, epidermis, and dermis at certain wavelengths. For

in vitro skin, they provided the values at 400 nm and 450-740 nm, with a step size of 10 nm. Regarding *in vitro* epidermis, they reported the absorption coefficient values at 400, 450, 500, 560, 600, 630, 650, 700, and 740 nm. They gave the reduced scattering coefficients for *in vitro* epidermis at the same wavelengths, except that they reported the values at 550 nm not 560 nm and that they provided the value at 633 nm in addition to the other values. As for the *in vitro* dermis, they specifically reported the absorption coefficient values for 400, 450, 500, 560, 600, 630, 650, 700, and 740 nm. They gave the reduced scattering coefficients for *in vitro* dermis at the same wavelengths, except that they reported the values at 550 nm not 560 nm and that they provided the value at 633 nm in addition to the other values.

For *in vivo* skin, arm, forehead, epidermis, and dermis, the authors reported the absorption coefficient at the same wavelength range. They also provided the reduced scattering coefficient of *in vivo* skin, arm, and forehead. For *in vivo* skin, they reported the absorption coefficient at 390-740 nm with a 10 nm step size, and they gave the reduced scattering coefficient at 360-740 nm with the same step size. Regarding the *in vivo* arm and *in vivo* forehead, they reported the absorption coefficient at 630, 660, and 700 nm, and they gave the reduced scattering coefficient at the same wavelengths, except that they also provided the value at 633 nm. As for *in vivo* epidermis and *in vivo* dermis, they gave the absorption coefficient at 360-740 nm with a step size of 10 nm.

Jacques (2013)

Jacques (2013) provided the anisotropy factor of the white matter, grey matter, skin, and skull at 500-1400 nm, the reduced scattering coefficient of the bone, skin, and brain at 250-2000 nm, and the absorption coefficient of subcutaneous fat at 400-1100 nm. Also, the author provided the

reduced scattering coefficient at 500 nm for the skin, brain, bone, dermis, epidermis, cortex of the frontal lobe, cortex of the temporal lobe, cerebral white mater, skull, and subcutaneous tissue.

Strangman, Li, and Zhang (2013)

Strangman et al. (2013) provided the mean absorption and scattering coefficients of the scalp, skull, cerebrospinal fluid, white matter, and grey matter between 690, 750, 780, and 830 nm.

Farina et al. (2015)

Farina et al. (2015) studied the optical coefficients of the human head. They had 9 subjects, and they collected optical data using different methods. They obtained the data using a continuous wave camera-based system, time-resolved broadband spectroscopy system, discrete wavelength time-resolved spectroscopy system, and single wavelength time-resolved spectroscopy system. The authors fitted the continuous wave data to an analytical solution of continuous wave reflectance of semi-infinite homogeneous medium using the diffusion approximation of the radiative transport equation. For time-resolved broadband spectroscopy and discrete wavelength time-resolved, the data was fitted to an analytical solution of 2-layered slab with semi-infinite lower layer using the diffusion equation, and the authors found that the best fit for the optical coefficients for these data was using the Levenberg-Marquardt algorithm. Regarding the single wavelength time-resolved data, it was fitted to an analytical solution of the diffusion approximation for a homogeneous diffusive sphere with the curvature of the head. The authors compared their fitted experimental data to Monte Carlo simulations of 3-layered laterally-infinite medium using the Beer-Lambert method. As a result of their work, they provided the absorption and reduced scattering coefficient of the head at 600-1000 nm.

Li, Zhao, Sun, and Li (2015)

Li et al. (2015) provided the absorption and scattering coefficients of the scalp, cerebrospinal fluid, skull, muscle, grey matter, white matter, arterial blood, and venous blood at 660, 810, and 980 nm. The authors also provide the anisotropy factor for the grey matter, arterial blood, and venous blood at these wavelengths. For the white matter, they provide the anisotropy factor at 660 nm and 810 nm.

Pitzschke et al. (2015)

Pitzschke et al. provided the absorption and reduced scattering coefficients of the skull, cerebrospinal flui, grey matter, white matter, pons, and thalamus at 671, 808, and over 671-808 nm.

Yue and Humayun (2015)

Yue and Humayun (2015) provided the absorption and reduced scattering coefficients of the scalp, skull, cerebrospinal fluid, white matter, and grey matter at 850 nm and 690 nm.

Yue et al. (2015)

Yue et al. (2015) provided the absorption and reduced scattering coefficients of the scalp, skull, cerebrospinal fluid, grey matter, and white matter at 850 nm.

Li, Xue, Wang, Li, and Wu (2017)

Li et al. (2017) provided the absorption and scattering coefficients of the scalp, cerebrospinal fluid, skull, muscle, grey matter, white matter, arterial blood, and venous blood at 660, 810, and 980 nm.

Materials and Methods

Materials

- MMC
- Matlab
- Ubuntu

Methods

In order to perform the simulations two head models were constructed using MMC based on Collins human adult brain imaged via magnetic resonance imaging (MRI). One head model was constructed using the optical properties of head biological tissues at 630 nm. The other one was created using the optical properties between 650 nm and 800 nm. Having two head models allows having simulations at various wavelengths. The constructed head was divided into four layers, a Scalp and head layer, a cerebrospinal fluid layer, a white matter layer, and grey matter layer. Further, in order to determine the optical properties of the head at the employed wavelength range, a comprehensive literature review of the optical properties for layers involved was performed, and an Excel file called “coefficients” attached to this report contains these results.

Moreover, one simulation was run using the 630 nm head model. The simulation illuminated the head with 30 million photons. In addition, four sets of simulations were performed using the second head model. One set of simulations varied the total number of photons illuminated (1k, 10k, 100k, and 1mill), the second one varied the wavelength used (650 nm, 750 nm, and 800nm), the third one varied power density (μW/cm2 and nW/cm2), and the fourth ran a previously employed clinical study device design at 785 nm.

The simulations included 29012391 RNG seeds and the head model was illuminated from the top of the head at the position of (75.7604835020458, 66.9948002207114, 168.218489512914) mm. Additionally, the direction vector of the source that illuminated the head with a pencil beam was [0.1636, 0.4569, -0.87435], and the simulation time was 3e-9 sec with a step gate of 2e-10. Also, one 2mm radius photon detector was used and positioned at (75.34, 79.89, 170.9) mm.

In order to construct the head models and specify the inputs for the simulations, MMC was run on Matlab. However, to run the simulations, Ubuntu was used, since the simulations required a windows Linux subsystem. After running the simulations and obtaining fluence data, the results were plotted using Matlab. The time at which the fluence results were plotted was specified to be 0.2 ns, allowing sufficient time for the photons to migrate through the head model and keeping the time constant to allow comparison between different simulations at the same time point.

Results

Head and Brain Mesh

The resulting head models that were constructed using MMC on Matlab are shown in **Figure 1**, which shows an outer view of the model depicting the head only, and **Figure 2** which shows both the head and the brain enclosed within.

Simulations Using 630 nm Head Model

The fluence profile of illuminating the 630 nm head model with 30million photons resulted in the greatest penetration depth of all the simulation (see **Table 7**). The photons migrated over a wide area in the head, and they scattered for 45 mm in the Z direction and 55 mm in the Y direction, showing that increasing photon number results in deeper penetration depth and wider scattering. In addition, for most of its propagation, the flux was higher than 4 mm^-2, indicating a high number of particles propagating the model at the given area and time.

Simulations Using 650-800nm Head Model

Simulations of Varying Photon Number

These simulations have shown that increasing photon number results in wider scattering and deeper propagation of light though the human head. Indeed, as **Table 7** shows, the scattering length in the Z direction was 25 mm and in the Y direction was 30 mm for the simulated 1k and 10k photons. However, it increased to 27 mm in the Z direction and 32 mm in the Y direction for the 100k simulation. Moreover, it further increased to 28 mm in the Z direction and 33 mm in the Y direction for the simulated 1mill photon migration. Although the difference is not high, an

increase in scattering and penetration is observed. More importantly, the flux also increases as the number of photons increases. Indeed, the flux magnitude for the simulated 1mill photon is mostly above 5 mm^-2 (see **Figure 8**). On the other hand, the flux for the 10k simulation varies nearly equally between 2 mm^-2 and 8 mm^-2.

Simulations of Various Wavelengths

The simulations of various wavelengths showed that increasing the wavelength, decreases scattering of light in the Y direction slightly but increases flux. Indeed, the length of propagation and scattering for the different wavelength simulations was constant at 25 mm. However, the length of propagation in the Y direction decreased from 32 mm for 650 nm to 30 mm for 750 nm and 27 mm for 800 nm (see **Table 7**). On the other hand, increasing wavelength increased flux. The flux for the 650 nm wavelength is nearly equivalently distributed between 4 mm^-2 and 8 mm^-2 (see **Figure 9**). But, for the 750 nm simulation, the flux is mostly larger than 6 mm^-2, and for the 800 nm simulation, the flux is mostly larger than 5 mm^-2 (see **Figure 10** & **11**).

Simulations of Various Power Density

Increasing power density resulted in higher propagation and scattering in both the Y and Z directions. Indeed, it increased from 23 mm in the Z direction and 25 mm in the Y direction for the μW/cm^2 simulation to 17 mm in the Z direction and 15 mm in the Y direction for the nW/cm2 (see **Table 7)**.

Simulations Using 785 nm Clinical Study Light Source

The simulation using this clinical study device design was not practical to be further perused using MMC because it required the simulation of 2.50E+21 photons as shown in **Equation 3**. Using these simulation inputs, the simulation was run on Ubuntu and for 1% of the simulation to be completed, 2hrs and 20 mins were required. This estimates 233.3 hrs for the completion of the whole simulation which was not feasible using MMC, since it does not function using a graphics card like Monte Carlo Extreme (MCX). Using a graphics card would make the simulation faster running more than 5 times the speed without a graphic card.

Time to Perform the Various Simulations

As seen in **Table 6**, running more photons takes more time, which is a limitation of MMC that does not run using a graphic card, as was mentioned earlier.

Discussion

Expected Clinical Results

Since the outer region of the brain is reached, some regeneration and cognitive improvement depending on source position are expected, if the energy level reaching the brain is higher than the threshold of energy needed to reach the brain to result in a positive impact. If the energy is higher than the threshold, regeneration in neurons and improvement in movement, sensation,

arithmetics, perception, spelling, and diction comprehension are expected. However, this threshold of energy is still unknown and is the focus of multiple research groups involved with photobiomodulation (see **Figure 12** for the known effects of light with different parameters on cells and tissue). To have a better estimate of the occurrence of improvement, the device parameters used in this project must be juxtaposed with those used in clinical photobiomodulation studies that yielded improvements in cognition. In addition, the simulations presented by this project must be compared with simulations of clinical NIR-emitting devices. Regarding these points, the parameters used in this project result in a lower total number of photons emitted (maximum of 10^9 photons) compared to clinical device parameters (around 10^21 photons and may be more or less). Moreover, using the simulations of this project, the photons reach around a maximum of 25%-30% deep in the brain. Interpolating this result, we estimate that photons from clinical devices reach more than 60% deep in the brain, stimulating deeper brain regions, such as the hypothalamus that is involved with memory. This corresponds with the results of clinical studies that report improvement in cognition and memory and executive function when the brain is illuminated by the clinical NIR-emitting devices (Salehpour et al., 2018).

Further, our total number of photons is also lower than that used in *in vitro* studies. However, we expect some improvements in cellular function, since the wavelength of light used in this project correspond to the optical window and is around 800 nm, which is found to be associated with better photobiomodulation (Salehpour et al., 2018). In comparison to *in vitro* studies performed at similar wavelength of around 800 nm (see **Table 9** to **11**), we expect an increase in adenosine triphosphate production, mitochondrial membrane potential, intracellular calcium levels, reactive oxygen species and nitric oxide levels below the harmful cellular levels, cell viability, and Akt

and Bcl-2 expression nNOS activity. On the other hand, expected decrease in NO donor SNAP-induced neuron death and caspase-3 expression (Salehpour et al., 2018).

Moreover, the result that photons were able to penetrate the head, reaching the cortex of the brain when only a small number of photons was simulated indicates that exposure to sun light while performing daily activities may have stimulatory effect on the brain, not only on bone. In addition, our results show that after 2 nsec, the flux of light has low values, which suggests that simulations and clinical device illumination may be performed for less than 2 nsec.

Application to Clinical Devices

Our results have shown that increasing photon number and power density increases light propagation and scattering. In addition, they have shown that increasing wavelength increases the flux. Applying our results to previously published clinical studies using transcranial NIR light-emitting devices, the 810 nm and 500 mW/cm2 device of Chaieb et al. should result in deeper light propagation and better neurological improvement than the device of Konstantinovic et al. that uses similar wavelength of 905 nm but smaller power density of 50mW/cm2 (see **Table 8**). Moreover, it is important to note that these previously clinical studies in addition to the simulations performed in this project do not result in severe skin heating, which should occur at 1 W/cm2 (Salehpour et al., 2018). Comparing wavelengths of previously published clinical studies, based on our results the device of Konstantinovic et al. should result in better performance than that of Salgado et al. because although it employs similar power density, it has a higher wavelength of 905 nm compared to 627 nm (see **Table 8**). Regarding photon number, comparing Barrett and Gonzales-Lima with Balnco et al., the device employed in Balnco et al.'s

should result in better performance because it runs for 8 mins allowing more photons to migrate through the head compared to that of Barrett and Gonzales-Lima that runs for only 4 mins.

Limitations

Among the limitations that should be confronted in the biomedical optics field in order to allow more simulations to be performed is the data limitation. As was seen in the *Optical Properties of the Human Head in the Literature* section, the optical properties available for the head layers are available in a small range of wavelengths, mainly at around 600-900 nm. In order for simulations to be performed at a wider range of wavelengths, the optical properties at these wavelengths, which function as inputs for the simulations, should be measured in vivo in the future. Further, one of the limitations of this project was using MMC which is time-consuming in regard to simulation time. As a solution, Monte Carlo Extreme may be used in the future since it is 5 times faster than MMC.

Conclusion

The significance of this project is that it set forth a clear set of guidelines for the specification of transcranial NIR-light emitting device parameters to result in the maximum penetration depth and flux through the head without exceeding the maximum permissible exposure of the skin. These in turn result in more neurological regeneration and better treatment of neurological disorders. These guidelines can be used by clinical studies and NIR light-emitting devices

manufacturers to optimize the performance of their devices toward resulting in further medical treatment.

In the future, graphic cards should be employed to simulate the devices used in previously published transcranial NIR light-emitting studies to reduce the time needed to run these simulations. Also, the optical properties of the head tissue at a wider wavelength range should be measured for these optical properties to be used as inputs in future simulations.

Acknowledgments

Gratitude and thanks are directed to the Creative Arts, Research, and Scholarship (CARAS) Program of Temple University for funding the project, Dr. Michel Lemay for reviewing this paper and providing helpful feedback, Mr. Yousef Hakim for his help with the significance and idea of the project and checking on the project's progress, Mr. Alexander Dumont for his help with using MMC and with coding, Mr. Brandon Harrison for his coordination of meetings about the project with Mr. Dumont and checking on the progress of the project, and Mr. Jerry So, Ms. Kavya Sreeram, Ms. Lynn Vorwick, Ms. Nina Mucciolo, Mr. Shahriar Rashvand, Mr. Shreyas Chandragiri, and Ms. Sunyu for their interest in and support for the project.

Appendices

Appendix A: Results

Head and Brain Mesh

Head Mesh

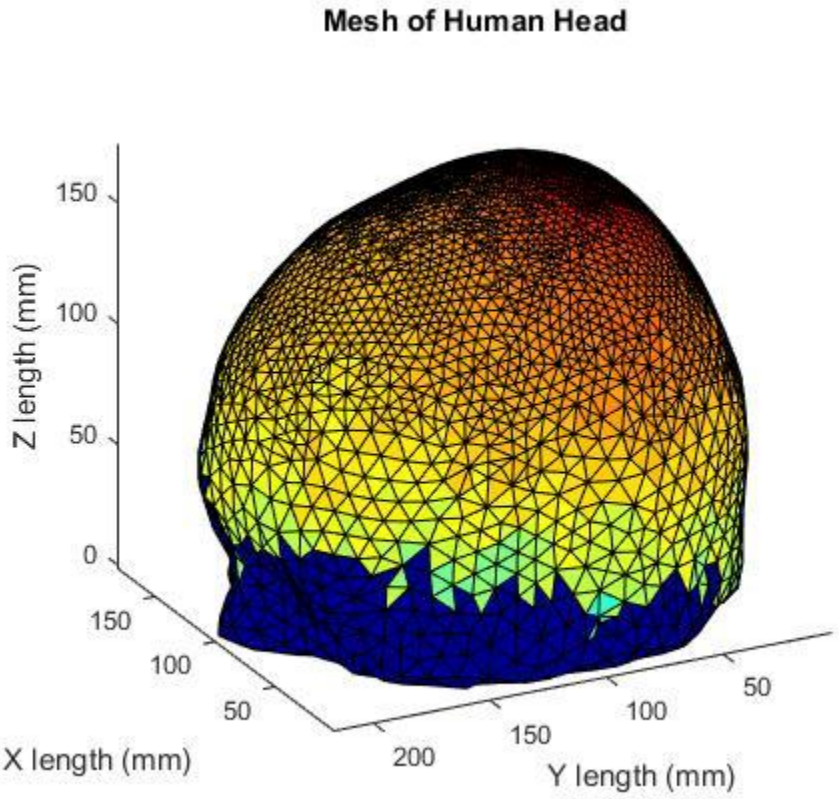

Figure 1: this shows an outer view of the created head mesh with brain enclosed.

Head with Brain Shown

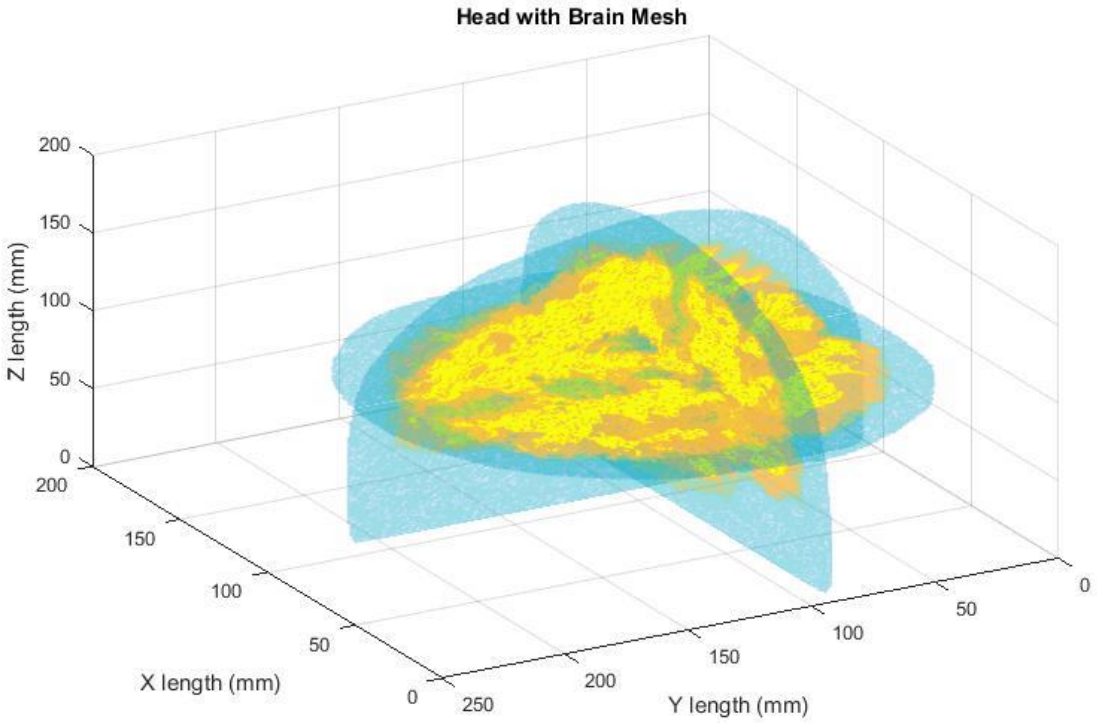

Figure 2: this shows the head model with its enclosed brain mesh employing slices from different planes.

Simulations Using 630 nm Head Model

Inputs for 630 nm Head Model

Tissue types	**μa (mm−1)**	**μs (mm−1)**	**Anisotropy Factor (g)**	**Refract. Index (n)**
Scalp & skull	0.019	7.8	0.89	1.37
CSF	0.004	0.009	0.89	1.37

Gray-matter	0.02	9	0.89	1.37
White-matter	0.08	40.9	0.84	1.37

Table 1: this shows the optical properties of human head tissue at 630 nm wavelength (Custo et al., 2006 & Yaroslavsky et al., 2002).

Fluence of Light at 630 nm Wavelength and 30 Million Photon

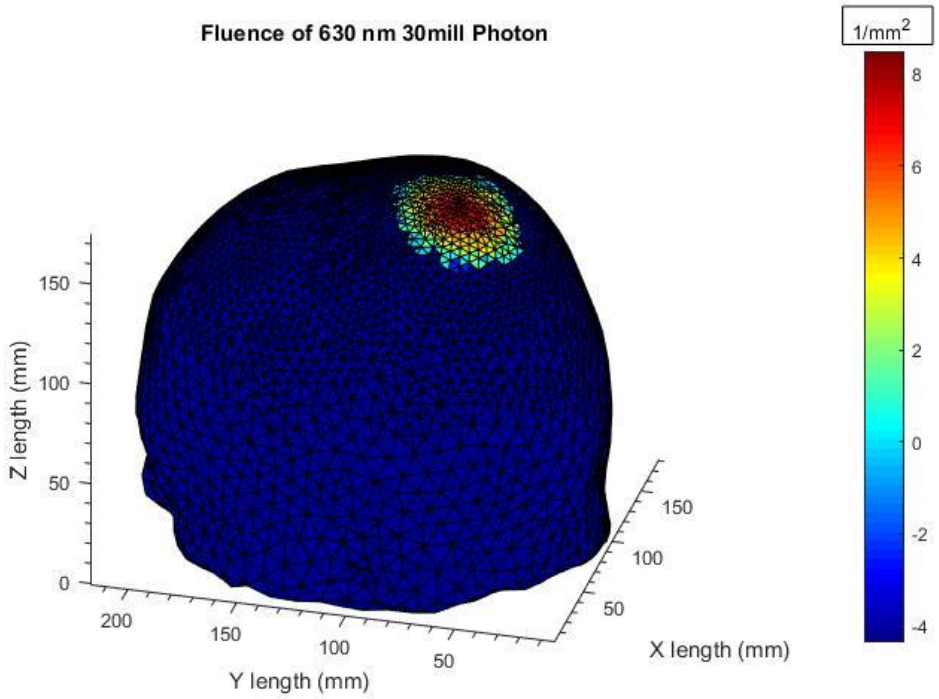

Figure 3: this shows the fluence of 630 nm wavelength light with 30 million photon through the head mesh. The color bar on the right shows the magnitude of flux.

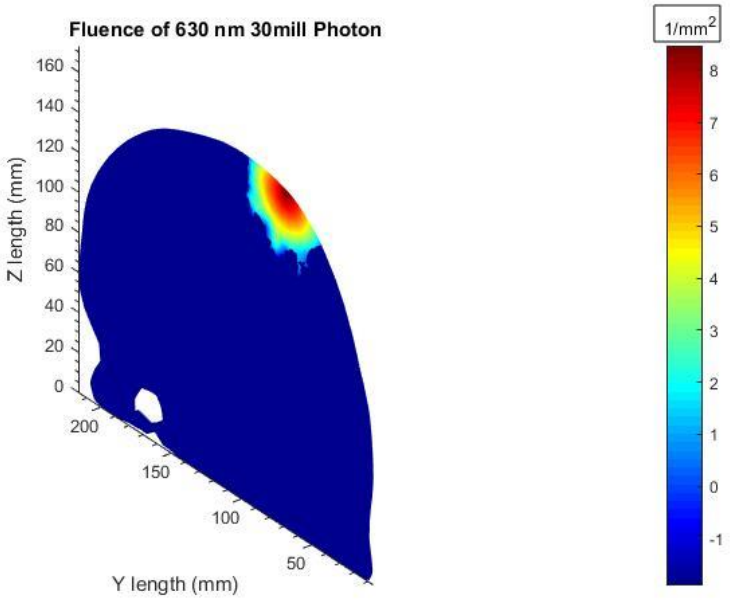

Figure 4: this shows the fluence of 630 nm wavelength light with 30 million photon through the a slice of the head mesh. The color bar on the right shows the magnitude of flux.

Simulations Using 650-800nm Head Model

Inputs for 650-800 nm Head Model

Tissue types	**μa (mm−1)**	**μs (mm−1)**	**Anisotropy Factor (g)**	**Refract. Index (n)**
Scalp & skull	0.017	17.5	0.9	1.58
Scalp	0.016	19	0.9	1.6
Skull	0.018	16	0.9	1.56
CSF	0.004	0.3	0	1.33

Gray-matter	0.09	21.5	0.9	1.4
White-matter	0.09	38.4	0.9	1.47

Table 2: this shows the optical properties of biological tissue between 650-800nm. The values for "Scalp and Skull" were obtained by averaging the coefficients for "Scalp" and "Skull," since their coefficients were close and the research paper did not provide "Scalp and Skull" values (Haeussinger et al., 2011).

Simulations of Varying Photon Number

- 1k Photon

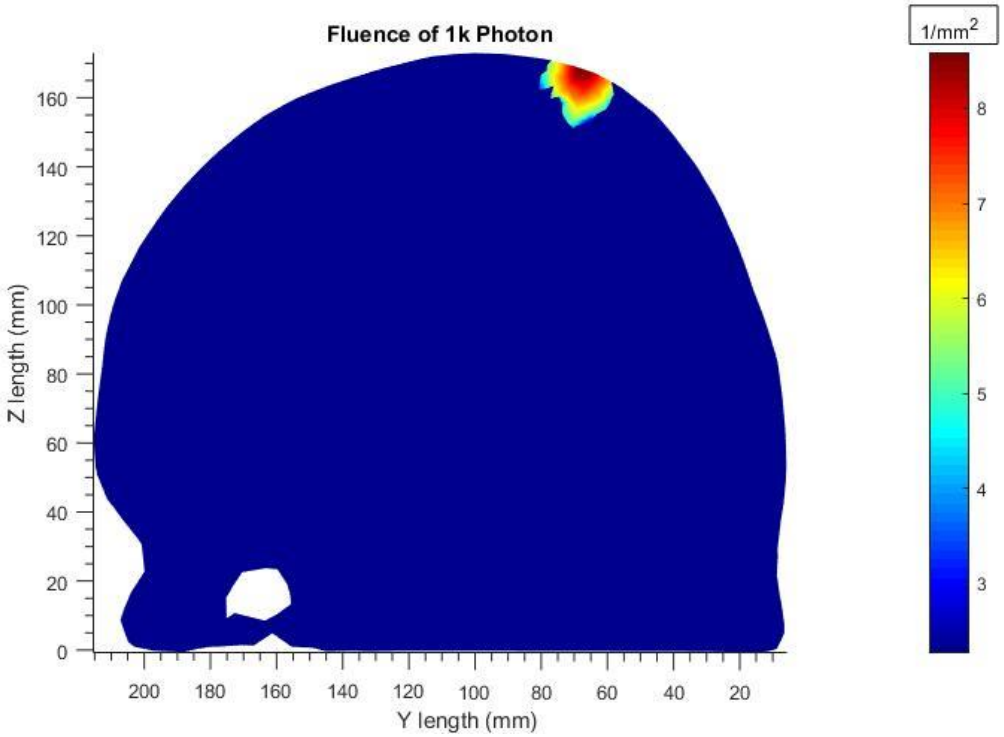

Figure 5: this shows the fluence of 1 thousand photon through the head mesh. The color bar on the right shows the magnitude of flux.

- 10k Photon

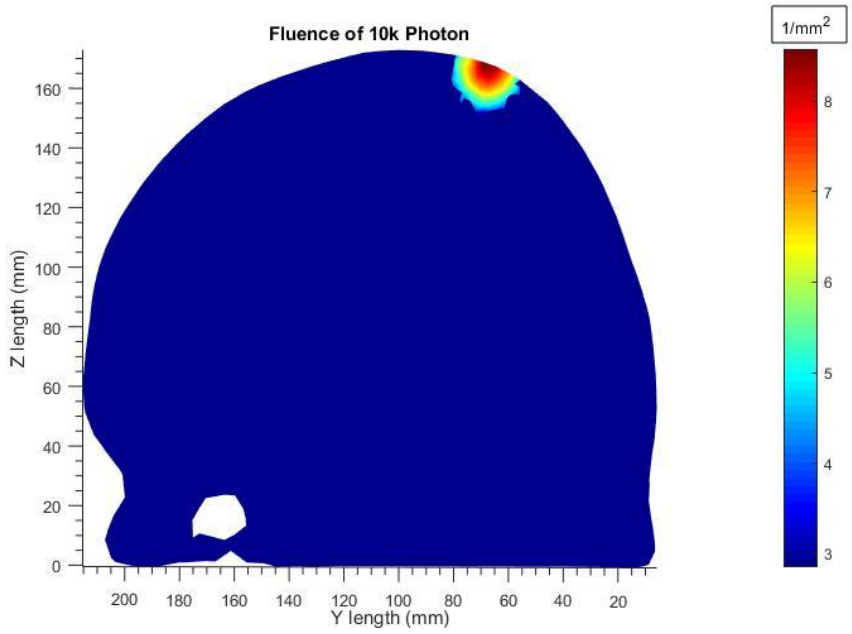

Figure 6: this shows the fluence of 10 thousand photon through the head mesh. The color bar on the right shows the magnitude of flux.

- 100k Photon

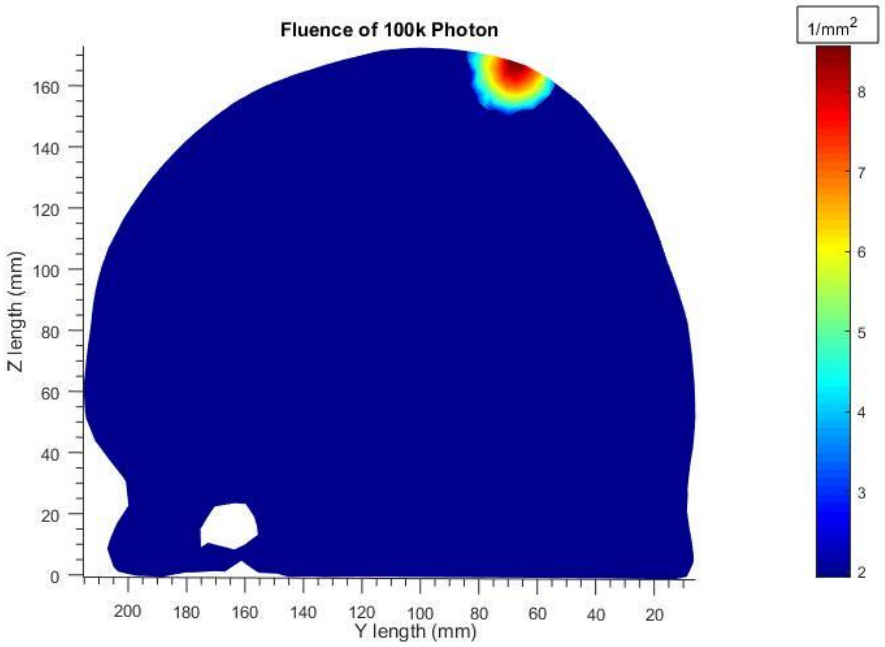

Figure 7: this shows the fluence of 100 thousand photon through the head mesh. The color bar on the right shows the magnitude of flux.

- 1million Photon

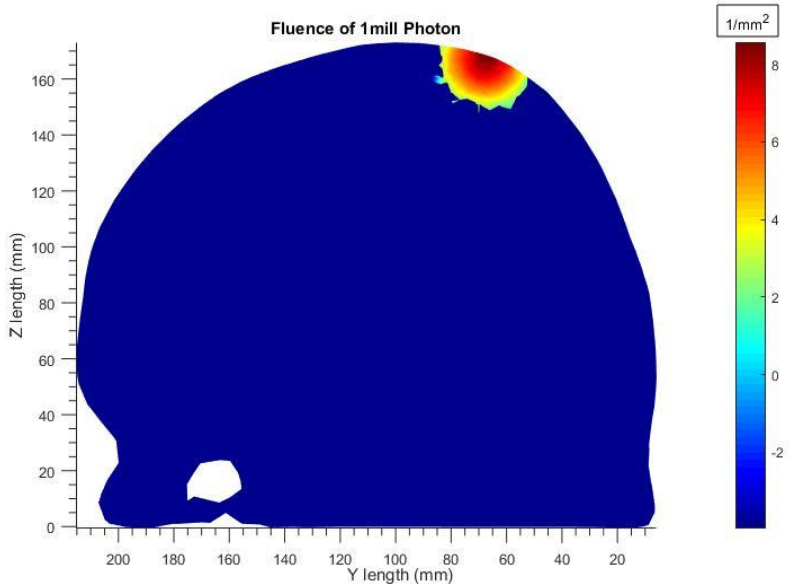

Figure 8: this shows the fluence of one million photon through the head mesh. The color bar on the right shows the magnitude of flux.

Simulations of Various Wavelengths

- Device Parameters

	650 nm	**750 nm**	**800 nm**
Power density or Intensity (W/cm^2)	1.00E-06	1.00E-06	1.00E-06
Area of Exposure (cm^2)	1.00E-04	1.00E-04	1.00E-04
Time (sec)	1.00E-04	1.00E-04	1.00E-04

Table 3: this shows the device illumination parameters used at the different simulated wavelengths.

- 650 nm Wavelength Light

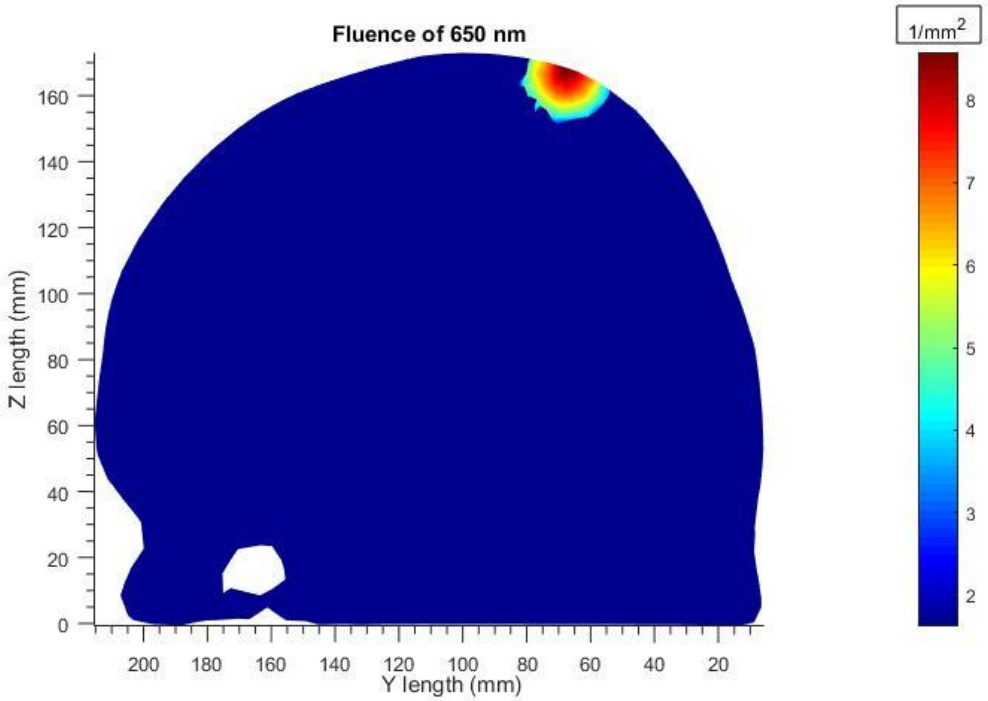

Figure 9: this shows the fluence of 650 nm wavelength light through the head mesh. The color bar on the right shows the magnitude of flux.

- 750 nm Wavelength Light

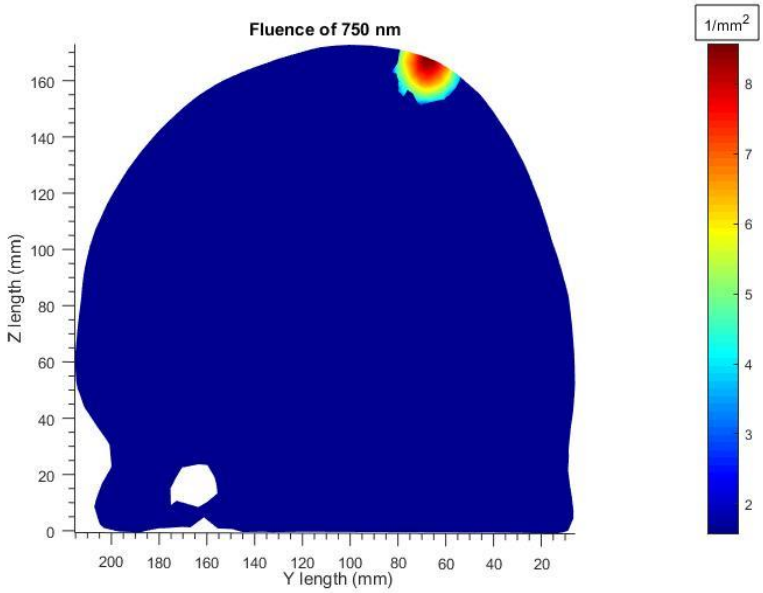

Figure 10: this shows the fluence of 750 nm wavelength light through the head mesh. The color bar on the right shows the magnitude of flux.

- 800 nm Wavelength Light

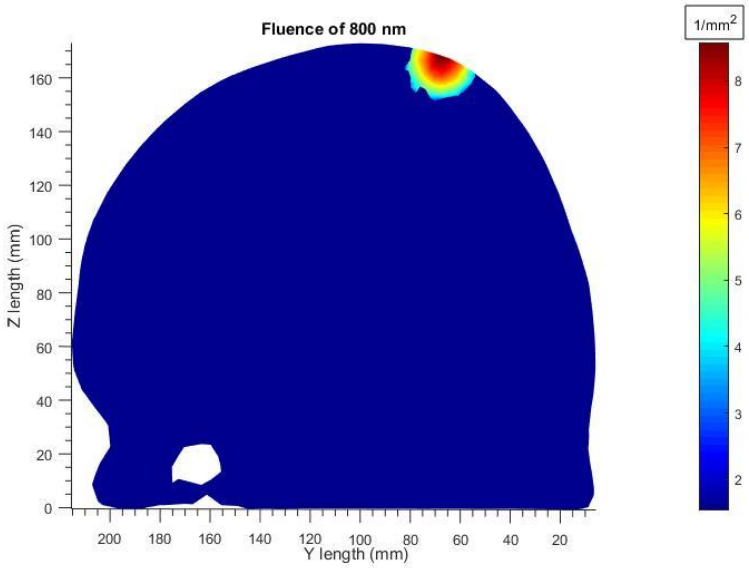

Figure 11: this shows the fluence of 800 nm wavelength light through the head mesh. The color bar on the right shows the magnitude of flux.

Simulations of Various Power Density

- Device Parameters

	µW/cm^2	nW/cm^2
Wavelength (nm)	700	700
Area of exposure (cm^2)	1.00E-04	1.00E-04

Time (sec)	1.00E-04	1.00E-04

Table 4: this shows the device illumination parameters used for the different power densities.

- nW/cm^2 Power Density Light

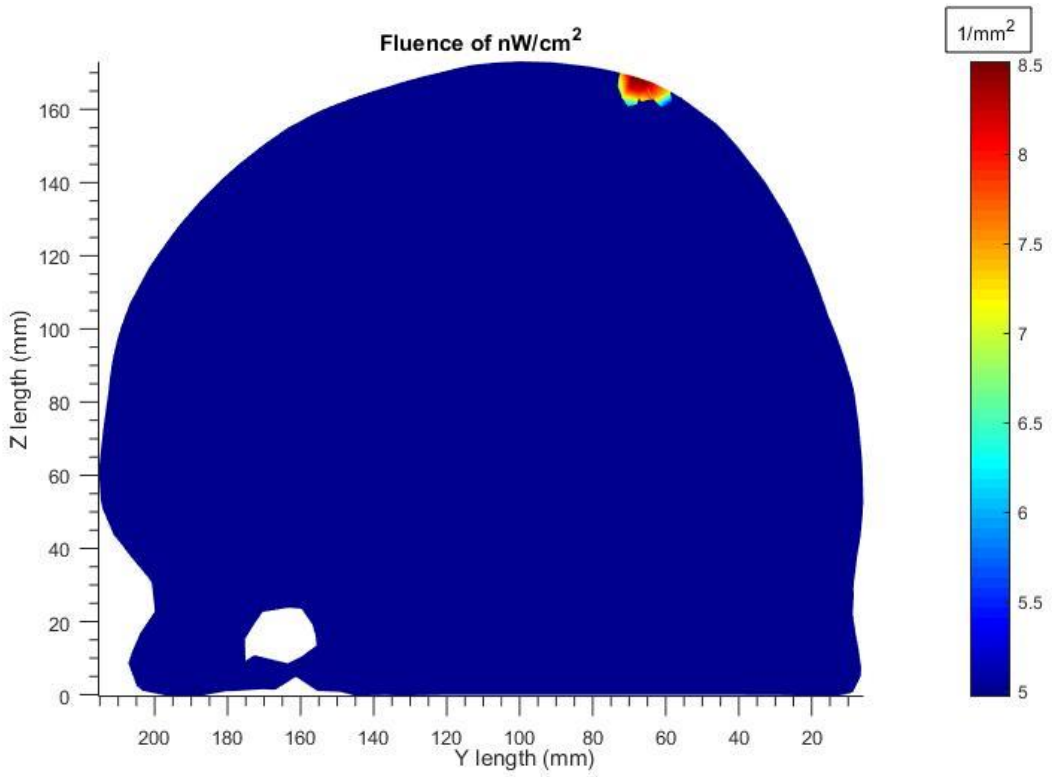

Figure 12: this shows the fluence of nW/cm^2 power density light through the head mesh. The color bar on the right shows the magnitude of flux.

- µW/cm^2 Power Density Light

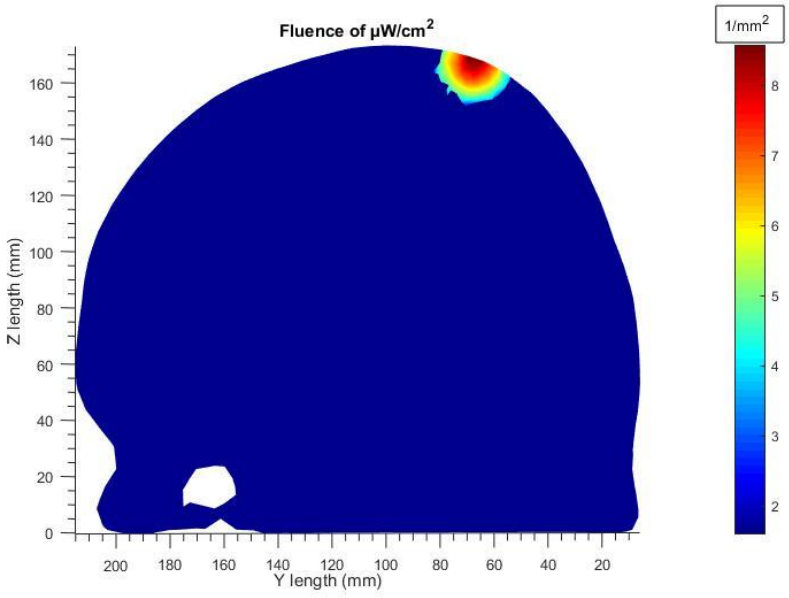

Figure 13: this shows the fluence of μW/cm^2 power density light through the head mesh. The color bar on the right shows the magnitude of flux.

Simulations Using 785 nm Clinical Study Light Source

- Parameters of the 785 nm Light Source

785 nm	
Power Level (W)	1.05
Time (min)	10
Photon Number	2.50E+21

Table 5: this shows the parameters of the 785 nm light-emitting device.

- Calculation for the Photons in the 785 nm Light Source

$$E = \frac{nhc}{\lambda} \quad ; \quad n = \frac{E\lambda}{hc}$$

Equations 1 & **2**: the first equation calculated the energy of the light based on the number of photons (n), Planck's constant (h), the speed of light (c), and wavelength (λ). The second equation is derived from the first, and it calculates the number of photons in light.

$$n = \frac{E\lambda}{hc} = \frac{(1050\ mW)(\frac{10^{-3}\ W}{1\ mW})(\frac{1\ \frac{J}{s}}{1\ W})(\frac{60\ s}{1\ min})(10\ \text{min})(785\text{x}10^{-9}\ m)}{6.626x10^{-34}\ Js\ (2.9979x10^{8}\ \frac{m}{s})} = 2.5x10^{21}\ photon$$

Equation 3: this shows the total number of photons in the 785 nm light source.

Time to Perform the Various Simulations

- Simulations' Time

Simulation	**Time for Simulation**
2.50E+21	2hrs 20mins for 1%
630 nm 30mill	1-4 hrs
1k	1 sec
10k	10 sec
100k	30 sec
1mill	2 min
650 nm	20sec

750 nm	20sec
800 nm	20sec
µW/cm^2	20sec
nW/cm^2	1 sec

Table 6: this shows the simulation time to perform the various simulations.

Light Penetration Lengths of the Simulations

Simulation	Z length Range (mm)	Z length (mm)	Y length Range (mm)	Y length (mm)
630 nm 30mill	130-175	45	40-95	55
1k	150-175	25	52-82	30
10k	150-175	25	50-80	30
100k	148-175	27	50-82	32
1mill	147-175	28	50-83	33
650 nm	150-175	25	50-82	32
750 nm	150-175	25	50-80	30
800 nm	150-175	25	55-82	27
µW/cm^2	152-175	23	55-80	25
nW/cm^2	158-175	17	55-70	15

Table 7: this shows the penetration depth of the propagated photons for the different simulations, showing the length of propagation in the Y and Z direction.

Appendix B: Discussion

Clinical NIR-Emitting Devices' Parameters

Study/year	Subjects (*n*)	Light source	Wavelengths	Irradiation parameters
Wu et al. 2012 [201]	Healthy volunteers (40)	Laser, 6 diodes, Advanced Chips & Products Corp. (Hillside, NJ, USA)	830 nm	7 mW per diode, 20 J/cm^2, 10 min, PW at 10 Hz with DC of 50%
Barrett and Gonzalez-Lima 2013 [44]	Healthy volunteers (40)	Laser, CG-5000, HD Laser Center (Dallas, TX, USA)	1064 nm	250 mW/cm^2, 60 J/cm^2, 4 min, one irradiation session, CW
Konstantinović et al. 2013 [202]	Healthy volunteers (14)	Laser, Endolaser 476, Enraf Nonius (Rotterdam, Netherlands)	905 nm	50 mW/cm^2, 3 J/cm^2 per site, 60 s, PW at 3000 Hz
Blanco et al. 2015 [45]	Healthy volunteers (30)	Laser, Cell Gen Therapeutics, LLC (Dallas, TX, USA)	1064 nm	250 mW/cm^2, 60 J/cm^2, 8 min, one irradiation session, CW
Chaieb et al. 2015 [203]	Healthy volunteers (55)	Laser, coupled with Weber Medical acupuncture	810 nm	500 mW/cm^2 at scalp via 4 laser needles, 10 min, one irradiation session, CW
Salgado et al. 2015 [125]	Healthy elderly women (25)	LEDs	627 nm	70 mW/cm^2, 10 J/cm^2, 30 s for each site (total of 4 sites), 2×/week for 4 weeks

Table 8: this shows the illumination parameters and number of subjects involved in different brain photobiomodulation studies (obtained from Salehpour et al., 2018).

Appendix C: Photobiomodulation on a Cellular and Tissue Level

In vitro Photobiomodulation

Study/year	Cell types	Light source	Wavelengths	Irradiation parameters	Findings
Oron et al. 2007 [116]	Cultured human neuronal cells	Laser, GaAs, Photothera, Inc. (Carlsbad, CA, USA)	808 nm	600 mW, 50 mW/cm^2, 0.05 J/cm^2, 1 s	Increased ATP content at 10 min post-irradiation
Sharma et al. 2011 [3]	Cultured mouse cortical neurons	Laser, Photothera, Inc. (Carlsbad, CA, USA)	810 nm	25 mW/cm^2; 0.03, 0.3, 3, 10, or 30 J/cm^2, single irradiation, CW	Highest increase in mitochondrial ROS (at 3 and 30 J/cm^2); increased intracellular NO (at 0.3 J/cm^2); increased MMP (at 0.3 and 3 J/cm^2); increased intracellular Ca^{2+} (at 3 J/cm^2); increased intracellular ATP (at 3 J/cm^2)
Fukuzaki et al. 2013 [140]	Human-derived glioblastoma cells	Laser, SUWTECH, LDC-2500 (China)	532 nm	60 mW, 845 mW/cm^2, 10.1, 20.3, or 30.4 × 10^2 J/cm^2; with corresponding duration of 20, 40, or 60 min; CW	Increased cell proliferation at 48 h post-irradiation through elevation of Akt expression mediated by suppression of PTEN production (at 20.3 and 30.4 × 10^2 J/cm^2)
Fukuzaki et al. 2015 [141]	Neural stem/progenitor cell derived	Laser, SUWTECH, LDC-2500 (China)	532 nm	60 mW, 845 mW/cm^2, 10.1, 20.3, or 30.4 × 10^2 J/cm^2; with corresponding duration of 20, 40 or 60 min; CW	Increased cell proliferation (at 30.4 × 10^2 J/cm^2); promoted migration of NSPCs through increased Akt expression
Yan et al. 2017 [28]	Dorsal root ganglion neurons	Laser, HN-1000, Laser Technology Application Research Institute (Guangzhou, China)	632.8 nm	12.74 mW/cm^2; 0.5, 1, 1.9, and 3.8 J/cm^2; with corresponding duration of 0.7, 1.25, 2.5, and 5 min in the dark, respectively; single irradiation, CW	Enhanced cell viability and neuritogenesis through induction of BDNF mRNA expression by increasing of Ca^{2+} influx, phosphorylated levels of CREB and ERK proteins
Duan et al. 2003 [142]	PC12 cell ($A\beta_{25-35}$-induced neurotoxicity)	LEDs, self-made GaAlAs	640 nm	0.05–1 mW/cm^2, 30–60 min, single irradiation, CW	At 0.09 mW/cm^2 and 60 min diminished apoptosis and attenuated DNA fragmentation
Yang et al. 2010 [137]	Primary astrocytes ($A\beta_{1-42}$-induced neurotoxicity)	Laser, He-Ne	632.8 nm	1.5 mW/cm^2, 16.2 J/cm^2, 3 h, single irradiation, CW	Decreased oxidative stress burden via suppression of superoxide anion production, NADPH oxidase; and phosphorylation of $cPLA_2$; inhibited pro-inflammatory markers including IL-1β and iNOS
Sommer et al. 2012 [110]	SH-EP and PC12 cells ($A\beta_{42}$-induced neurotoxicity)	Laser	670 nm	17.36 mW/cm^2, 1 J/cm^2, 1 min, single irradiation, PW at 1 Hz	Increased ATP levels in $A\beta_{42}$-free SH-EP cells SH-EP cells: reduced intracellular $A\beta_{42}$ aggregate amounts; increased cell proliferation PC12 cells: small decrease in ATP levels in $A\beta_{42}$-challenged
Liang et al. 2012 [143]	SH-SY5Y, PC12, and HEK293T cells ($A\beta_{25-35}$-induced neurotoxicity)	Laser, HN-1000 (Guangzhou, China)	632.8 nm	12.74 mW/cm^2, 2 J/cm^2, single irradiation, CW	In all cell types: decreased apoptosis via Akt/GSK3b/b-catenin pathway
Meng et al. 2013 [144]	SH-SY5Y cell and mice hippocampal primary neuron ($A\beta_{25-35}$ and $A\beta_{1-42}$-induced neurotoxicity)	Laser, HN-1000, Laser Technology Application Research Institute (Guangzhou, China)	632.8 nm	12.74 mW/cm^2; 0.5, 1, 2, or 4 J/cm^2; with corresponding duration of 0.7, 1.25, 2.5, and 5 min in the dark, respectively; single irradiation, CW	At 2 J/cm^2: promoted cell survival and improved dendrite growth atrophy through up-regulation of BDNF mediated by activation of ERK/CREB signaling pathway
Duggett and Chazot 2014 [48]	Cath.a-differentiated cells ($A\beta_{1-42}$-induced neurotoxicity)	LEDs, Virulite Distribution Ltd. (UK)	1068 nm	5 mW/cm^2, 5 sets of 3 min irradiation (with 30-min interval) for 3 days, PW at 600 Hz, with DC of 300μs	Decreased cell death (3.5–25 μM of $A\beta_{42}$)
Trimmer et al. 2009 [111]	PD cybrid cells	Laser, Acculaser, PhotoThera, Inc. (Carlsbad, CA, USA)	810 nm	50 mW/cm^2, 2 J/cm^2, 40 s, single irradiation, CW	Increased total distance traveled and velocity of mitochondria at 2 h post-irradiation
Wong-Riley et al. 2001 [107]		LEDs, GaAlAs	670 nm	50 mW/cm^2, 4 J/cm^2, 80 s, CW	

Table 9: this shows in vitro photobiomodulation results (obtained from Salehpour et al., 2018).

Study/year	Cell types	Light source	Wavelengths	Irradiation parameters	Findings
	Cultured rat cortical neurons (TTX-induced neurotoxicity)				Increased CCO activity in all three metabolic categories of neurons (daily irradiation for 5 days); increased CCO activity in darkly reactive cell type (a single irradiation)
Wong-Riley et al. 2005 [106]	Cultured rat visual cortical neurons (KCN-induced neurotoxicity)	LEDs, Quantum Devices, Inc. (Barnaveld, WI, USA)	670, 728, 770, 830, or 880 nm	50 mW/cm^2, 4 to 30 J/cm^2, 80 to 600 s, CW	670 and 830 nm significantly increased CCO activity and ATP content back to control levels compared to 728, 880, and 770 nm (each at 4 J/cm^2) 670 nm: pre-irradiation at 30 J/cm^2 reduced cell death
Liang et al. 2006 [24]	Cultured rat visual cortical neurons (KCN-induced neurotoxicity)	LEDs, Quantum Devices, Inc. (Barnaveld, WI, USA)	670 nm	50 mW/cm^2, 30 J/cm^2, single irradiation, CW	Pre-irradiation reduced cell death (100 μM of KCN) and (300 μ M of KCN); reduced number of ssDNA-positive neurons (100 μ M of KCN) and (300 μ M of KCN); reduced caspase-3 and Bax levels, and increased Bcl-2 levels (both 100 and 300 μ M of KCN); reduced ROS production (300 μ M of KCN)
Liang et al. 2008 [138]	Cultured rat occipital cortical and striatal neurons (KCN- or MMP$^+$- or rotenone-induced neurotoxicity)	LEDs, Quantum Devices, Inc. (Barnaveld, WI, USA)	670 nm	50 mW/cm^2, 4 J/cm^2, 80 s, 1 to 4×/day, CW	KCN: reduced apoptosis (1 irradiation) and (2 irradiations); reduced ROS production (2, 3, and 4 irradiations); reduced NO production (2 and 3 irradiations); reduced nitrotyrosine expression (2 irradiations); highest increase in CCO activity and ATP level (2 irradiations) MPP$^+$: twice a day irradiation suppressed ROS and NO generation, increased ATP level and attenuated apoptosis in both types of neurons Rotenone: twice a day irradiation reduced apoptosis, ROS and NO levels, and increased ATP level in both types of neurons
Ying et al. 2008 [109]	Cultured rat visual cortical and striatal neurons (Rotenone- or MPP$^+$-induced neurotoxicity)	LEDs, Quantum Devices, Inc. (Barnaveld, WI, USA)	670 nm	50 mW/cm^2, 4 J/cm^2, 80 s, CW	Rotenone: LED irradiation and pre-irradiation decreased apoptosis in both types of neurons; MPP$^+$: LED irradiation and pre-irradiation decreased apoptosis in both types of neurons; LED irradiation and pre-irradiation increased ATP content in striatal neurons
Giuliani et al. 2009 [145]	PC12 cell (H_2O_2-induced neurotoxicity)	Laser, SANYO DL3149-055A, (RGM, Genoa, Italy)	670 nm	0.005 or 0.011 mW/cm^2; 0.11, 0.22, 5.06 or 10.12 J/cm^2; 20 or 900 s, single irradiation, PW at 100 Hz with DC of 1% or 50%	Enhanced axonal protection via stimulation of NGF-induced neurite outgrowth; rescued MMP (at all fluencies); increased cell viability (at 0.11 and 0.22 J/cm^2)
Huang et al. 2013 [33]	Cultured mouse cortical neurons (H_2O_2- or $CoCl_2$- or rotenone-induced neurotoxicity)	Laser, Photothera, Inc. (Carlsbad, CA, USA)	810 nm	20 mW/cm^2; 3 J/cm^2, 150 s, single irradiation, CW	Increased cell viability (at 10 and 20 μM of H_2O_2, 0.2, 0.5, 1, and 2 mM of $CoCl_2$, and 0.2, 2, and 5 μM of rotenone); decreased mitochondrial and cytoplasmic ROS production, and increased MMP (at 500 μ M of $CoCl_2$, 20 μM of H_2O_2, and 200 nM of rotenone)
Dong et al. 2015 [115]			830 nm	0.1, 0.5, 1, 3, or 10 J/cm^2, CW	

Table 10: this shows *in vitro* photobiomodulation results (obtained from Salehpour et al., 2018).

Study/year	Cell types	Light source	Wavelengths	Irradiation parameters	Findings
	Cultured SH-SY5Y cells ($CoCl_2$-induced neurotoxicity)	LEDs, PhotoMedex (Horsham, PA, USA)			Increased cell viability and ATP production (at 3 and 10 J/cm^2); decreased lactate production at 18 h post-toxin treatment (at 3 J/cm^2); decreased ROS production and increased MMP; reduced cytochrome c leakage and diminished caspase-3 activation; suppressed apoptosis (at 3 J/cm^2)
Choi et al. 2012 [146]	Cultured rat cortical neurons (OGD-induced neurotoxicity)	LEDs, QRAY, Inc. (Seoul, Korea)	710 nm	50 mW/cm^2, 4 J/cm^2, 4 min, 1 to 4× within 8 h at 2-h intervals for 7 days, CW	Enhanced cell protection; promoted neurite outgrowth and synaptogenesis mediated by MAPK activation
Yu et al. 2015 [139]	Cultured mouse cortical neurons (OGD-induced neurotoxicity)	Laser, Photothera, Inc. (Carlsbad, CA, USA)	810 nm	25 mW/cm^2, 0.3 J/cm^2, 2 min, single irradiation, CW	Decreased NO production and nNOS activity (at 5 and 30 min post-irradiation); decreased NO donor SNAP-induced neuron death; promoted Akt and Bcl-2 expression (at 1 and 2 h); ameliorated Bax and BAD expression (at 1 and 2 h); suppressed caspase-3 and cleaved caspase-3 expression (at 2 h)

Table 11: this shows *in vitro* photobiomodulation results (obtained from Salehpour et al., 2018).

Effect of Light on Cells and Tissue

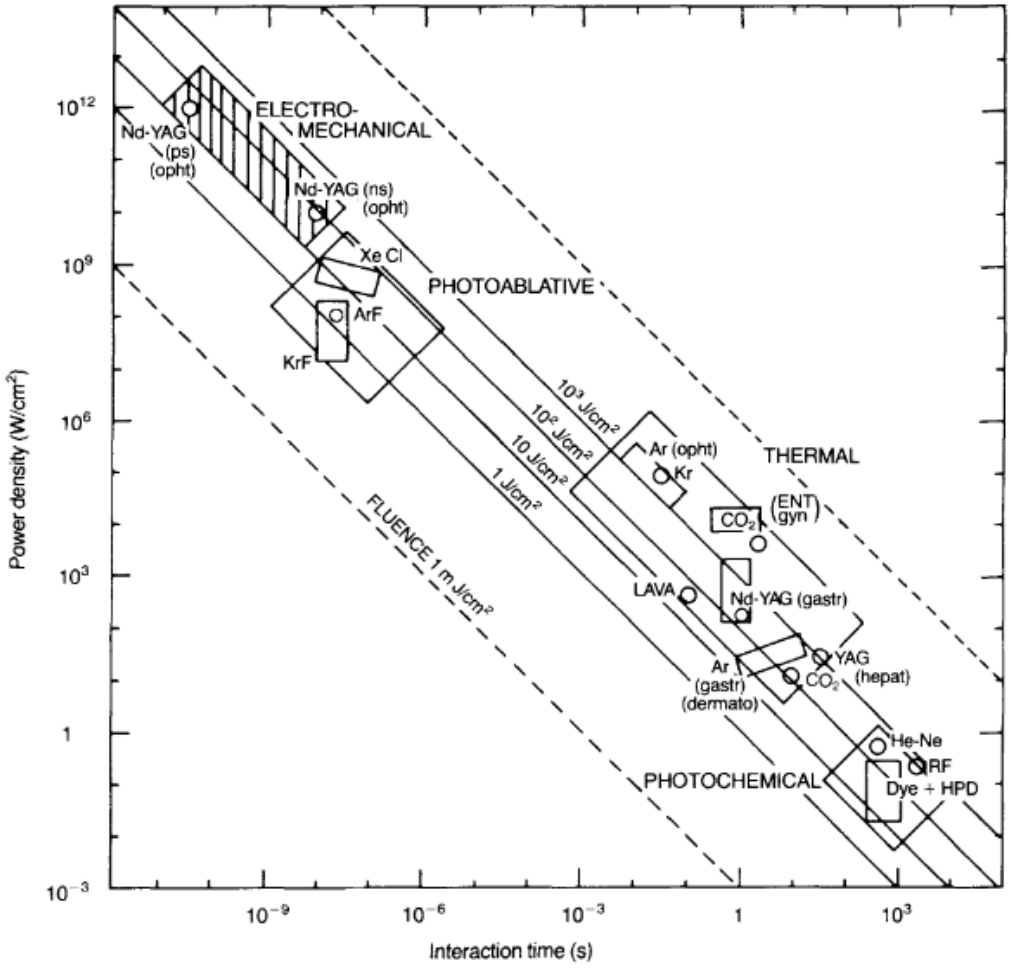

Figure 12: this shows the effect of light illumination on cells and tissue based on fluence, irradiance, time of illumination, and type of light source used (Boulnois, 1986).

References

Anderson, R. R., & Parrish, J. A. (1981). The optics of human skin. *Journal of investigative dermatology*, *77*(1), 13-19.

Bashkatov, A. N., Genina, E. A., Kochubey, V. I., & Tuchin, V. V. (2005). Optical properties of human skin, subcutaneous and mucous tissues in the wavelength range from 400 to 2000 nm. *Journal of Physics D: Applied Physics*, *38*(15), 2543.

Bashkatov, A. N., Genina, E. A., Kochubey, V. I., & Tuchin, V. V. (2006, July). Optical properties of human cranial bone in the spectral range from 800 to 2000 nm. In *Saratov Fall Meeting 2005: Optical Technologies in Biophysics and Medicine VII* (Vol. 6163, p. 616310). International Society for Optics and Photonics.

Bashkatov, A. N., Genina, E. A., & Tuchin, V. V. (2011). Optical properties of skin, subcutaneous, and muscle tissues: a review. *Journal of Innovative Optical Health*

Sciences, *4*(01), 9-38.

Bevilacqua, F., Piguet, D., Marquet, P., Gross, J. D., Tromberg, B. J., & Depeursinge, C. (1999). In vivo local determination of tissue optical properties: applications to human brain. *Applied optics*, *38*(22), 4939-4950.

Boas, D. A., & Dale, A. M. (2005). Simulation study of magnetic resonance imaging–guided cortically constrained diffuse optical tomography of human brain function. *Applied optics*, *44*(10), 1957-1968.

Boulnois, J. L. (1986). Photophysical processes in recent medical laser developments: a review. *Lasers in medical science*, *1*(1), 47-66.

Chan, E. K., Sorg, B., Protsenko, D., O'Neil, M., Motamedi, M., & Welch, A. J. (1996). Effects of compression on soft tissue optical properties. *IEEE Journal of selected topics in quantum electronics*, *2*(4), 943-950.

Cheong, W. F., Prahl, S. A., & Welch, A. J. (1990). A review of the optical properties of biological tissues. *IEEE journal of quantum electronics*, *26*(12), 2166-2185.

Comelli, D., Bassi, A., Pifferi, A., Taroni, P., Torricelli, A., Cubeddu, R., Martelli, F., & Zaccanti, G. (2007). In vivo time-resolved reflectance spectroscopy of the human forehead. *Applied optics*, *46*(10), 1717-1725.

Custo, A., Wells Iii, W. M., Barnett, A. H., Hillman, E. M., & Boas, D. A. (2006). Effective

scattering coefficient of the cerebral spinal fluid in adult head models for diffuse optical imaging. *Applied optics*, *45*(19), 4747-4755.

Ding, H., Lu, J. Q., Wooden, W. A., Kragel, P. J., & Hu, X. H. (2006). Refractive indices of human skin tissues at eight wavelengths and estimated dispersion relations between 300 and 1600 nm. *Physics in Medicine & Biology*, *51*(6), 1479.

Dögnitz, N., & Wagnières, G. (1998). Determination of tissue optical properties by steady-state spatial frequency-domain reflectometry. *Lasers in medical science*, *13*(1), 55-65.

Doornbos, R. M. P., Lang, R., Aalders, M. C., Cross, F. W., & Sterenborg, H. J. C. M. (1999). The determination of in vivo human tissue optical properties and absolute chromophore concentrations using spatially resolved steady-state diffuse reflectance spectroscopy. *Physics in Medicine & Biology*, *44*(4), 967.

Fang, Q. (2010). Mesh-based Monte Carlo method using fast ray-tracing in Plücker coordinates. *Biomedical optics express*, *1*(1), 165-175.

Farina, A., Torricelli, A., Bargigia, I., Spinelli, L., Cubeddu, R., Foschum, F., Jäger, M., Simon, E., Fugger, O., Kienle, A., & Martelli, F. (2015). In-vivo multilaboratory investigation of the optical properties of the human head. *Biomedical optics express*, *6*(7), 2609-2623.

Firbank, M., Hiraoka, M., Essenpreis, M., & Delpy, D. T. (1993). Measurement of the optical properties of the skull in the wavelength range 650-950 nm. *Physics in Medicine &*

Biology, *38*(4), 503.

Firbank, M., Okada, E., & Delpy, D. T. (1998). A theoretical study of the signal contribution of regions of the adult head to near-infrared spectroscopy studies of visual evoked responses. *Neuroimage*, *8*(1), 69-78.

Franceschini, M. A., & Boas, D. A. (2004). Noninvasive measurement of neuronal activity with near-infrared optical imaging. *Neuroimage*, *21*(1), 372-386.

Fukui, Y., Ajichi, Y., & Okada, E. (2003). Monte Carlo prediction of near-infrared light propagation in realistic adult and neonatal head models. *Applied optics*, *42*(16), 2881 2887.

Gebhart, S. C., Lin, W. C., & Mahadevan-Jansen, A. (2006). In vitro determination of normal and neoplastic human brain tissue optical properties using inverse adding-doubling. *Physics in Medicine & Biology*, *51*(8), 2011.

Graaff, R., Dassel, A. C. M., Koelink, M. H., De Mul, F. F. M., Aarnoudse, J. G., & Zijlstra, W. G. (1993). Optical properties of human dermis in vitro and in vivo. *Applied optics*, *32*(4), 435-447.

Haeussinger, F. B., Heinzel, S., Hahn, T., Schecklmann, M., Ehlis, A. C., & Fallgatter, A. J. (2011). Simulation of near-infrared light absorption considering individual head and prefrontal cortex anatomy: implications for optical neuroimaging. *PloS one*, *6*(10),

e26377.

Iino, K., Maruo, K., Arimoto, H., Hyodo, K., Nakatani, T., & Yamada, Y. (2003). Monte Carlo simulation of near infrared reflectance spectroscopy in the wavelength range from 1000 nm to 1900 nm. *Optical review*, *10*(6), 600-606.

Jacques, S. L., Alter, C. A., & Prahl, S. A. (1987). Angular dependence of HeNe laser light scattering by human dermis. *Lasers Life Sci*, *1*(4), 309-333.

Jacques, S. L. (2013). Optical properties of biological tissues: a review. *Physics in Medicine & Biology*, *58*(11), R37.

Koyama, T., Iwasaki, A., Ogoshi, Y., & Okada, E. (2005). Practical and adequate approach to modeling light propagation in an adult head with low-scattering regions by use of diffusion theory. *Applied optics*, *44*(11), 2094-2103.

Kurihara, K., Kawaguchi, H., Obata, T., Ito, H., Sakatani, K., & Okada, E. (2012). The influence of frontal sinus in brain activation measurements by near-infrared spectroscopy analyzed by realistic head models. *Biomedical optics express*, *3*(9), 2121-2130.

Lister, T., Wright, P. A., & Chappell, P. H. (2012). Optical properties of human skin. *Journal of biomedical optics*, *17*(9), 090901.

Li, T., Gong, H., & Luo, Q. (2011). Visualization of light propagation in visible Chinese human head for functional near-infrared spectroscopy. *Journal of biomedical optics*, *16*(4),

045001.

Li, T., Xue, C., Wang, P., Li, Y., & Wu, L. (2017). Photon penetration depth in human brain for light stimulation and treatment: A realistic Monte Carlo simulation study. *Journal of Innovative Optical Health Sciences*, *10*(05), 1743002.

Li, T., Zhao, Y., Sun, Y., & Li, K. (2015). Effects of wavelength, beam type and size on cerebral low-level laser therapy by a Monte Carlo study on visible Chinese human. *Journal of Innovative Optical Health Sciences*, *8*(01), 1540002.

Mansouri, C., L'Huillier, J. P., Kashou, N. H., & Humeau, A. (2010). Depth sensitivity analysis of functional near-infrared spectroscopy measurement using three-dimensional Monte Carlo modelling-based magnetic resonance imaging. *Lasers in medical science*, *25*(3), 431-438.

Marchesini, R., Bertoni, A., Andreola, S., Melloni, E., & Sichirollo, A. E. (1989). Extinction and absorption coefficients and scattering phase functions of human tissues in vitro. *Applied Optics*, *28*(12), 2318-2324.

Matcher, S. J., Cope, M., & Delpy, D. T. (1997). In vivo measurements of the wavelength dependence of tissue-scattering coefficients between 760 and 900 nm measured with time-resolved spectroscopy. *Applied Optics*, *36*(1), 386-396.

Meglinsky, I. V., & Matcher, S. J. (2001). Modelling the sampling volume for skin blood

oxygenation measurements. *Medical and Biological Engineering and Computing*, *39*(1), 44-50.

Mudra, R. M., Nadler, A., Keller, E., & Niederer, P. F. (2006). Analysis of near-infrared spectroscopy and indocyanine green dye dilution with Monte Carlo simulation of light propagation in the adult brain. *Journal of biomedical optics*, *11*(4), 044009.

Okada, E., & Delpy, D. T. (2003, 1). Near-infrared light propagation in an adult head model. I. Modeling of low-level scattering in the cerebrospinal fluid layer. *Applied optics*, *42*(16), 2906-2914.

Okada, E., & Delpy, D. T. (2003, 2). Near-infrared light propagation in an adult head model. II. Effect of superficial tissue thickness on the sensitivity of the near-infrared spectroscopy signal. *Applied optics*, *42*(16), 2915-2921.

Okada, E., Firbank, M., Schweiger, M., Arridge, S. R., Cope, M., & Delpy, D. T. (1997). Theoretical and experimental investigation of near-infrared light propagation in a model of the adult head. *Applied optics*, *36*(1), 21-31.

Pitzschke, A., Lovisa, B., Seydoux, O., Zellweger, M., Pfleiderer, M., Tardy, Y., & Wagnières, G. (2015). Red and NIR light dosimetry in the human deep brain. *Physics in Medicine & Biology*, *60*(7), 2921.

Popp, A. K., Valentine, M. T., Kaplan, P. D., & Weitz, D. A. (2003). Microscopic origin of light

scattering in tissue. *Applied optics*, *42*(16), 2871-2880.

Rajadhyaksha, M., González, S., Zavislan, J. M., Anderson, R. R., & Webb, R. H. (1999). In vivo confocal scanning laser microscopy of human skin II: advances in instrumentation and comparison with histology1. *Journal of Investigative Dermatology*, *113*(3), 293-303.

Salehpour, F., Mahmoudi, J., Kamari, F., Sadigh-Eteghad, S., Rasta, S. H., & Hamblin, M. R. (2018). Brain Photobiomodulation Therapy: a Narrative Review. *Molecular neurobiology*, 1-36.

Salomatina, E. V., Jiang, B., Novak, J., & Yaroslavsky, A. N. (2006). Optical properties of normal and cancerous human skin in the visible and near-infrared spectral range. *Journal of biomedical optics*, *11*(6), 064026.

Sandell, J. L., & Zhu, T. C. (2011). A review of in-vivo optical properties of human tissues and its impact on PDT. *Journal of biophotonics*, *4*(11-12), 773-787.

Schneiderheinze, D. H., Hillman, T. R., & Sampson, D. D. (2007). Modified discrete particle model of optical scattering in skin tissue accounting for multiparticle scattering. *Optics express*, *15*(23), 15002-15010.

Simpson, C. R., Kohl, M., Essenpreis, M., & Cope, M. (1998). Near-infrared optical properties of ex vivo human skin and subcutaneous tissues measured using the Monte Carlo inversion technique. *Physics in Medicine & Biology*, *43*(9), 2465.

Splinter, R., Cheong, W. F., van Gemert, M. J., & Welch, A. J. (1989). In vitro optical properties of human and canine brain and urinary bladder tissues at 633 nm. *Lasers in surgery and medicine*, *9*(1), 37-41.

Sterenborg, H. J. C. M., Van Gemert, M. J. C., Kamphorst, W., Wolbers, J. G., & Hogervorst, W. (1989). The spectral dependence of the optical properties of human brain. *Lasers in medical science*, *4*(4), 221-227.

Strangman, G. E., Li, Z., & Zhang, Q. (2013). Depth sensitivity and source-detector separations for near infrared spectroscopy based on the Colin27 brain template. *PloS one*, *8*(8), e66319.

Tauber, S., Baumgartner, R., Schorn, K., & Beyer, W. (2001). Lightdosimetric quantitative analysis of the human petrous bone: Experimental study for laser irradiation of the cochlea. *Lasers in Surgery and Medicine: The Official Journal of the American Society for Laser Medicine and Surgery*, *28*(1), 18-26.

Tearney, G. J., Brezinski, M. E., Southern, J. F., Bouma, B. E., Hee, M. R., & Fujimoto, J. G. (1995). Determination of the refractive index of highly scattering human tissue by optical coherence tomography. *Optics letters*, *20*(21), 2258-2260.

Troy, T. L., & Thennadil, S. N. (2001). Optical properties of human skin in the near infrared wavelength range of 1000 to 2200 nm. *Journal of biomedical optics*, *6*(2), 167-177.

Tseng, S. H., Grant, A., & Durkin, A. J. (2008). In vivo determination of skin near-infrared optical properties using diffuse optical spectroscopy. *Journal of biomedical optics*, *13*(1), 014016.

Van der Zee, P. (1992). Measurement and modelling of the optical properties of human tissue in the near infrared (Doctoral dissertation, University of London).

Van Gemert, M. J. C., Jacques, S. L., Sterenborg, H. J. C. M., & Star, W. M. (1989). Skin optics. *IEEE Transactions on biomedical engineering*, *36*(12), 1146-1154.

Yaroslavsky, A. N., Schulze, P. C., Yaroslavsky, I. V., Schober, R., Ulrich, F., & Schwarzmaier, H. J. (2002). Optical properties of selected native and coagulated human brain tissues in vitro in the visible and near infrared spectral range. *Physics in Medicine & Biology*, *47*(12), 2059.

Yue, L., & Humayun, M. S. (2015). Monte Carlo analysis of the enhanced transcrania penetration using distributed near-infrared emitter array. *Journal of biomedical optics*, *20*(8), 088001.

Yue, L., Monge, M., Ozgur, M.H., Murphy, K., Louie, S., Miller, C.A., Emami, A. & Humayun, M.S. (2015, March). Simulation and measurement of transcranial near infrared light penetration. In *Optical Interactions with Tissue and Cells XXVI* (Vol. 9321, p. 93210S). International Society for Optics and Photonics.